The miniJPAS survey: the photometric redshift catalogue

A. Hernán-Caballero[1]*, J. Varela[2], C. López-Sanjuan[2], D. Muniesa[1], T. Civera[1], J. Chaves-Montero[3],
L. A. Díaz-García[4], J. Laur[5], C. Hernández-Monteagudo[6,7], R. Abramo[8], R. Angulo[3], D. Cristóbal-Hornillos[1],
R. M. González Delgado[4], N. Greisel[1], A. Orsi[1], C. Queiroz[8,9], D. Sobral[10], A. Tamm[5], E. Tempel[5],
H. Vázquez-Ramió[2], J. Alcaniz[11], N. Benítez[4], S. Bonoli[1,3,12], S. Carneiro[13], J. Cenarro[2], R. Dupke[11,14,15],
A. Ederoclite[16], A. Marín-Franch[2], C. Mendes de Oliveira[16], M. Moles[1,4], L. Sodré Jr.[16], K. Taylor[17], E. S. Cypriano[16],
and G. Martínez-Solaeche[4]

[1] Centro de Estudios de Física del Cosmos de Aragón (CEFCA), Plaza San Juan, 1, E-44001 Teruel, Spain
[2] Centro de Estudios de Física del Cosmos de Aragón (CEFCA), Unidad Asociada al CSIC, Plaza San Juan, 1, E-44001 Teruel, Spain
[3] Donostia International Physics Centre, Paseo Manuel de Lardizabal 4, E-20018 Donostia-San Sebastian, Spain
[4] Instituto de Astrofísica de Andalucía (CSIC), P.O. Box 3004, E-18080 Granada, Spain
[5] Tartu Observatory, University of Tartu, Observatooriumi 1, 61602 Tõravere, Estonia
[6] Departamento de Astrofísica, Universidad de La Laguna, E-38206 La Laguna, Tenerife, Spain
[7] Instituto de Astrofísica de Canarias, E-38200 La Laguna, Tenerife, Spain
[8] Instituto de Física, Universidade de São Paulo, Rua do Matão 1371, CEP 05508-090, São Paulo, Brazil
[9] Departamento de Astronomia, Instituto de Física, Universidade Federal do Rio Grande do Sul (UFRGS), Av. Bento Gonçalves 9500, Porto Alegre, R.S, Brazil
[10] Department of Physics, Lancaster University, Lancaster, LA1 4YB, UK
[11] Observatório Nacional, Ministério da Ciência, Tecnologia, Inovação e Comunicações, Rua General José Cristino, 77, São Cristóvão, 20921-400, Rio de Janeiro, Brazil
[12] Ikerbasque, Basque Foundation for Science, E-48013 Bilbao, Spain
[13] Instituto de Física, Universidade Federal da Bahia, 40210-340, Salvador, BA, Brazil
[14] Department of Astronomy, University of Michigan, 311 West Hall, 1085 South University Ave., Ann Arbor, USA
[15] Department of Physics and Astronomy, University of Alabama, Box 870324, Tuscaloosa, AL, USA
[16] Departamento de Astronomia, Instituto de Astronomia, Geofísica e Ciências Atmosféricas da USP, Cidade Universitária, 05508-900, São Paulo, SP, Brazil
[17] Instruments4

ABSTRACT

MiniJPAS is a ~1 deg^2 imaging survey of the AEGIS field in 60 bands, performed to demonstrate the scientific potential of the upcoming Javalambre-Physics of the Accelerating Universe Astrophysical Survey (J-PAS). Full coverage of the 3800–9100 Å range with 54 narrow-band filters, in combination with 6 optical broad-band filters, allow for extremely accurate photometric redshifts (photo-z), which applied over areas of thousands of square degrees will enable new applications of the photo-z technique such as measurement of baryonic acoustic oscillations. In this paper we describe the method used to obtain the photo-z included in the publicly available miniJPAS catalogue, and characterise the photo-z performance. We build 100 Å resolution photo-spectra from the PSF-corrected forced-aperture photometry. Systematic offsets in the photometry are corrected by applying magnitude shifts obtained through iterative fitting with stellar population synthesis models. We compute photo-z with a customised version of LePhare, using a set of templates optimised for the J-PAS filter-set. We analyse the accuracy of miniJPAS photo-z and their dependence on multiple quantities using a subsample of 5,266 galaxies with spectroscopic redshifts from SDSS and DEEP, that we find to be representative of the whole r<23 miniJPAS sample. Formal 1-σ uncertainties for the photo-z that are calculated with the $\Delta\chi^2$ method underestimate the actual redshift errors. The *odds* parameters has the stronger correlation with $|\Delta z|$, and accurately reproduces the probability of a redshift outlier ($|\Delta z|$>0.03) irrespective of the magnitude, redshift, or spectral type of the sources. We show that the two main summary statistics characterising the photo-z accuracy for a population of galaxies (σ_{NMAD} and η) can be predicted by the distribution of *odds* in such population, and use this to estimate them for the whole miniJPAS sample. At r<23 there are ~17,500 galaxies per deg^2 with valid photo-z estimates, of which ~4,200 are expected to have $|\Delta z|$<0.003. The typical error is σ_{NMAD}=0.013 with an outlier rate η=0.39. The target photo-z accuracy σ_{NMAD}=0.003 is achieved for *odds*>0.82 with η=0.05, at the cost of decreasing the density of selected galaxies to n~5,200 deg^{-2} (of which ~2,600 have $|\Delta z|$<0.003).

Key words. methods: data analysis - catalogues - galaxies: distances and redshifts - galaxies: photometry

1. Introduction

The idea of using multi-wavelength photometry to estimate the redshift of galaxies (photometric redshifts, photo-z in the fol-

* email: ahernan@cefca.es

lowing) was first proposed as a last resort technique to obtain redshifts for sources deemed too faint for spectroscopy to be feasible or economical (Baum 1962; Couch et al. 1983). Photo-*z* became increasingly useful with the advent of deep multi-wavelength imaging surveys, starting with the Hubble Deep Field (e.g. Lanzetta et al. 1996; Mobasher et al. 1996; Fernández-Soto et al. 1999). The main advantage of photo-*z* over spectroscopic redshifts (spec-*z*) is the ability to obtain redshifts for all the sources detected in an imaging survey without preselection. Combined with large CCD detectors, this implies an increase in the survey speed of orders of magnitude compared to the most advanced multi-object spectrographs (Blake & Bridle 2005).

The main drawback of the photo-*z* method is the accuracy of its redshift estimates, typically much lower compared to spec-*z*, imposing hard constraints on their range of application. However, in the last few years photo-*z* techniques have matured enough to promote a shift in the redshift strategy of many current and upcoming surveys, which now have photo-*z* as their primary method for distance determination. Spectroscopy is still essential for obtaining calibration and validation samples needed to fine-tune the photo-*z* machinery, or to follow up on particularly interesting sources. However, relying on photo-*z* for an overwhelming majority of targets allows for complete, flux-limited samples containing many millions of galaxies, which opens up entirely new applications such as baryonic acoustic oscillation (BAO) measurements (Blake & Bridle 2005; Angulo et al. 2008; Chaves-Montero et al. 2018).

Essential to this rise to preeminence of photo-*z* has been their huge improvement in accuracy and reliability over time, in particular on imaging surveys designed with photo-*z* in mind, which split the optical range into increasingly large numbers of ever narrower bandpasses. The first wide-area survey of the photo-*z* era was the Sloan Digital Sky Survey (SDSS; York et al. 2000), with only 5 (carefully designed) broadband filters. COMBO-17 (Wolf et al. 2003) and Subaru COSMOS 20 (Taniguchi et al. 2007, 2015) raised the number of filters to 17 and 20, respectively, including broad- and medium- or narrow-band filters. The Advanced, Large, Homogeneous Area, Medium- Band Redshift Astronomical1 (ALHAMBRA) survey (Moles et al. 2008) observed ~4 deg² in 20 optical medium-band filters (FWHM~300 Å) combined with JHKs near-infrared imaging. The Survey for High-z Absorption Red and Dead Sources (SHARDS; Pérez-González et al. 2013) imaged the Hubble Deep Field in 25 contiguous optical filters with FWHM~170 Å, and the Physics of the Accelerating Universe Survey (PAUS) observed the COSMOS field in 40 filters with FWHM~130 Å (Eriksen et al. 2019).

A new landmark of the application of photo-*z* will be reached with the Javalambre-Physics of the Accelerating Universe Astrophysical Survey (J-PAS; Benítez et al. 2009, 2014), specifically designed to achieve the high redshift accuracy required to perform BAO measurements over a wide redshift range. Using 54 narrow-band filters (FWHM~145 Å) complemented with two broadband filters at both extremes of the optical range, J-PAS imaging will effectively obtain a low-resolution spectrum (photo-spectrum) for every 0.46″pixel in the sky over thousands of square degrees. The J-PAS survey will be performed by the 2.5-m Javalambre Survey Telescope (JST), equipped with a 1.2 Gigapixel camera (JPCam) with a field of view of 4.2 deg².

To test the performance of JST and begin scientific operation prior to the installation of JPCam, a pathfinder camera (PF) with a single 9k x 9k CCD was installed. To prove the scientific potential of J-PAS, a small survey of ~1 deg² (miniJPAS) was carried out with PF on the AEGIS field using the 56 J-PAS filters as well as 4 broadband filters (*u*, *g*, *r*, *i*). MiniJPAS observations span 4 overlapping pointings along the Extended Groth Strip (EGS), reaching the depth planned for J-PAS (5-σ limits between ~21.5 and 22.5 for the narrow-band filters and ~24 for the broad-band filters in a 3″aperture). A detailed description of the miniJPAS observations, data reduction, and calibration is presented in Bonoli et al. (2020, hereafter **B21**). Fully reduced images and source catalogues are publicly available at the CE-FCA catalogues portal.[1]

In this paper, we present the photometric redshift catalogue for miniJPAS. Section 2 outlines the miniJPAS observations and data reduction, and describes the photometric measurements used for photo-*z* calculation and the spectroscopic redshifts. Section 3 discusses our photometric recalibration procedure. Section 4 offers an overview of the photo-*z* code, the templates used, and its outputs, while Sect. 5 discusses the sources of error in photo-*z* estimates. In Sect. 6, we present the main results on the redshift distribution and photo-*z* accuracy for miniJPAS galaxies and its dependence on multiple quantities. Finally, Sect. 7 summarises our conclusions. All magnitudes are presented in the AB system.

2. Data

2.1. observations and data reduction

The observations and data reduction of miniJPAS are described in detail in Sect. 2 and Sect. 3 of **B21**. Here we provide a brief summary. The miniJPAS covers the EGS in 4 overlapping pointings, for a total area of ~1 deg². Each pointing was observed with a minimum of 4 exposures per filter, with a dithering of 10″along both CCD axes. The readout of the CCD was done in 2×2 binning mode for the narrow-band filters (0.46″ pix^{-1}) and 1×1 for broad-band (0.23″ pix^{-1}). Individual exposure times were 120 s for the 56 narrow-band filters as well as the *u* filter, but only 30 s for the other broadband filters to prevent saturation. Total exposure times range from 480 s to 3240 s, depending on the filter and pointing (see Table A.1 in **B21** for details).

Data reduction for the individual images includes the standard bias and over-scan subtraction, trimming, flat fielding, and illumination correction. Also, some issues specific to the Pathfinder camera (which unlike JPCam, was not designed specifically for the JST/T250) required additional corrections for vignetting, background patterns, and fringing (see **B21**).

Astrometric calibration was performed with Sᴄᴀᴍᴘ (Bertin 2006) using the Gaia DR2 catalogue as reference. The astrometric solution for the individual images has a rms of ~0.035″with respect to Gaia. Coaddition of the individual images was performed with Sᴡᴀʀᴘ (Bertin et al. 2002), with all the images resampled to the fiducial pixel scale of the camera (0.23″).

The average 5-σ depth of the coadded narrow-band images ranges from ~21.5-22.0 AB magnitudes in the reddest filters to ~22.5-23.5 in the bluest ones. For broad-band filters, it is *u*~22.8, *g*~24.0, *r*~23.8, and *i*~23.2.

The PSF FWHM of the coadded images ranges from ~0.6″to ~2.0″, with most of them below the 1.5″mark. The images for the reference band (*r*) have the lowest PSF FWHM, averaging 0.7″in the four pointings.

---

[1] http://archive.cefca.es/catalogues/minijpas-pdr201912

2.2. Photometry

Source detection and extraction on the reduced miniJPAS images was performed with SExtractor (Bertin & Arnouts 1996). Aperture photometry was obtained in both dual-mode and single-mode for several types and aperture sizes and calibrated using an adaptation of the method presented in López-Sanjuan et al. (2019b, see Sects. 3.3 and 3.4 in B21 for details).

In dual-mode, the extraction aperture is defined in a reference band (in our case the detection band *r*) and used to perform forced photometry on the images in all the other filters). SExtractor computes total magnitudes using the auto (MAG_AUTO), isophotal (MAG_ISO), and Petrosian (MAG_PETRO) apertures. These apertures are defined individually for each source based on the *r* band so that the fraction of the (estimated) total flux of the galaxy enclosed is constant, irrespective of the galaxy size and surface brightness profile. A constant scaling factor then converts the fluxes integrated in the apertures to total fluxes.

However, accurate total fluxes are much less important than accurate colour indices for the purpose of photo-*z* estimation. Obtaining accurate colours requires to maximise the signal-to-noise ratio (S/N) within the extraction aperture and to compensate for PSF variation among the images in different filters. In order to achieve this, we use PSF corrected magnitudes (MAG_PSFCOR) obtained following the method presented in Molino et al. (2019), which is based on ColorPro (Coe et al. 2006).

Very briefly, PSFCOR magnitudes are obtained by extracting the flux in a small aperture, defined as the Kron aperture (Kron 1980) with semi-major axis equal to 1 Kron radius in the reference band. This is half the size of a standard AUTO aperture in SExtractor (2 Kron radii). The resulting magnitude is known as the "restricted AUTO" or just "restricted" magnitude (Molino et al. 2017, 2019). For the reference band, the PSFCOR magnitude is simply the restricted magnitude. For bands with wider PSF than the reference band, a correction term for PSF broadening is applied, as follows:

$$\text{PSFCOR}_j = \text{REST}_j + \text{REST}_r - \text{REST}(j)_r \qquad (1)$$

where REST_j and REST_r are the magnitudes measured on the restricted aperture for the images in band *j* and the reference band, respectively, while $\text{REST}(j)_r$ is measured on the reference image after convolution to the same PSF of the image in band *j*.

If, on the contrary, band *j* has a narrower PSF compared to the reference band, then the PSFCOR magnitude is simply the restricted magnitude measured on the image after convolution to the same PSF of the reference band. We emphasise that PSFCOR magnitudes are not total magnitudes. They underestimate the total flux of galaxies by ~0.5 mag, on average, with respect to AUTO magnitudes (see also González Delgado et al. 2021).

Hereafter, we will omit the explicit reference to the aperture type when discussing magnitudes, colours, or magnitude offsets. Unless otherwise stated, it will be implicit that AUTO magnitudes are used whenever the flux or luminosity in a single band is needed (e.g.: selection of a flux-limited sample, redshift priors) while PSFCOR magnitudes are used for SED fitting and colour-dependent quantities.

The photometry is corrected for atmospheric extinction as part of the calibration process (see López-Sanjuan et al. 2019b, for details). We also correct for Galactic extinction using the Milky Way dust maps from Bayestar17 (Green et al. 2018) with
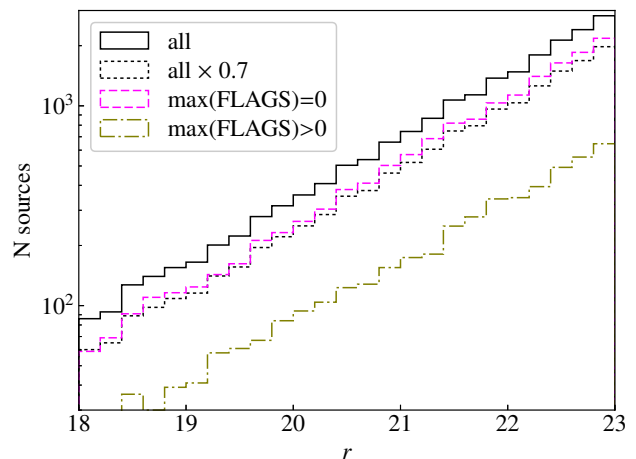
Fig. 1. Distribution of *r*-band magnitudes for the whole miniJPAS sample (black solid line), flagged sources (olive dot-dashed line), and non-flagged sources (magenta dashed line). The distribution for the whole sample scaled by a factor 0.7 is shown for reference (black dotted line).

extinction coefficients k_λ computed using the prescription in Whitten et al. (2019) for the extinction law of Schlafly et al. (2016).

2.3. Flags

The miniJPAS catalogue includes the column FLAGS, which contains information on whether each source is affected, in each of the bands, by a number of issues that may impair or invalidate the photometry. The FLAGS value is an integer that encodes several binary flags (see B21 for the details), including the SExtractor flags (which alert for close neighbours, blending, saturation, truncation, etc) as well as two additional flags that mark sources duplicated in another tile or that are known to be variable. Sources that have no apparent issues in their photometry in a particular band have FLAGS=0 for that band. Sources with FLAGS>0 in at least one band represent ~30% of the miniJPAS catalogue.

We compute photo-*z* for every source brighter than *r*<24 and with FLAGS<4 in the detection band (this removes saturated and truncated sources as well as those with incomplete or corrupted data in the extraction aperture). The FLAGS values are used to choose which bands are considered for the photo-*z* calculation. In the general case, we select only those bands with FLAGS=0 (meaning none of the SExtractor flags or additional flags is raised). However, if a source has FLAGS>0 in more than 50% of the bands, we relax this condition by requiring FLAGS<4, which dismisses the values indicating close neighbours or blending.

The impact of the photometric issues signalled by the flags on the photo-*z* accuracy is hard to predict as it depends on many factors, including the specific bands affected, the error introduced in the photometric measurement, the SED of the source, and its redshift. In general, the photo-*z* accuracy is degraded in sources with flags, and, in particular, the rate of catastrophic errors (outliers) is substantially higher.

Except for saturation, all the conditions signaled by the photometry flags depend mainly on the location of the source within the image, not its intrinsic properties. As a consequence, which sources are flagged should not depend on their brightness, apparent size, redshift, or spectral type. Figure 1 confirms this to
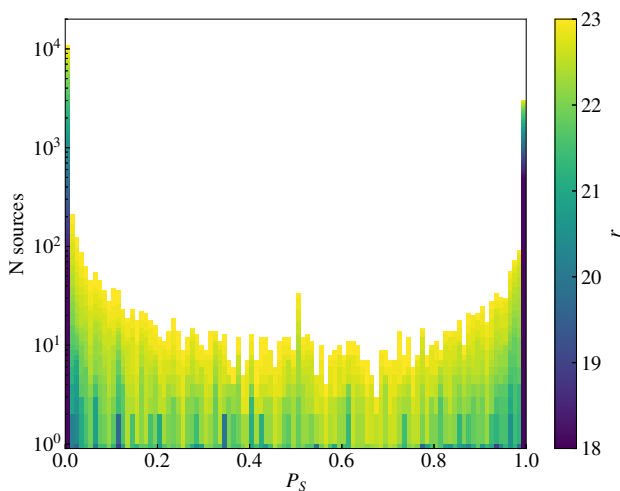
Fig. 2. Distribution of the probability of being a star, P_S, for miniJPAS sources as a function of the (colour-coded) limiting magnitude of the sample. The spike at $P_S=0.5$ is due to sources with insufficient S/N for classification in the detection band, which get $P_S=0.5$ by default.

actually be the case for brightness, with ~30% of sources being flagged irrespective of their magnitude.

Because of this, we consider the ~70% of sources with no flags to be representative of the full miniJPAS sample. We will use this sub-sample to discuss the properties of the population of miniJPAS sources throughout the paper.

2.4. Star/galaxy classification

The miniJPAS catalogue includes the results of different methods for separating stars from galaxies. The most basic approach is the CLASS_STAR parameter from SEXTRACTOR, which compares the spatial profile of the source with the expectation for a point source. A more realistic morphological classification is given by MORPH_PROB_STAR which gives the probability of a source being a star given its spatial profile and a prior probability based on its r-band magnitude (see López-Sanjuan et al. 2019a, for details). TO-TAL_PROB_STAR combines MORPH_PROB_STAR with parallax information from Gaia for a more robust determination. Finally, ERT_PROB_STAR provides classification using the Extremely Randomised Trees machine learning method, which uses morphological and photometric parameters (Baqui et al. 2020).

Although ERT_PROB_STAR has the highest success rate in separating stars from galaxies (Bonoli et al. 2020; Baqui et al. 2020), we choose TOTAL_PROB_STAR as the preferred measurement of the probability of being a star, P_S, through the paper. This is because TOTAL_PROB_STAR has the advantage of not relying on the SED of the galaxy, which is important for obtaining the redshift distribution of galaxies in a consistent way, as we show below.

The distribution of P_S is strongly bimodal, with most sources concentrated near the extremes of its range, at $P_S \sim 0$ (very likely to be a galaxy) or $P_S \sim 1$ (star, see Fig. 2). In particular, 96.8% of the sources brighter than $r=22$ have either $P_S < 0.01$ or $P_S > 0.99$. However, at faint magnitudes the distinction becomes more uncertain, with many sources taking intermediate values of P_S. As a consequence, applying a cut in P_S to tell apart galaxies from stars results in contamination and incompleteness in both
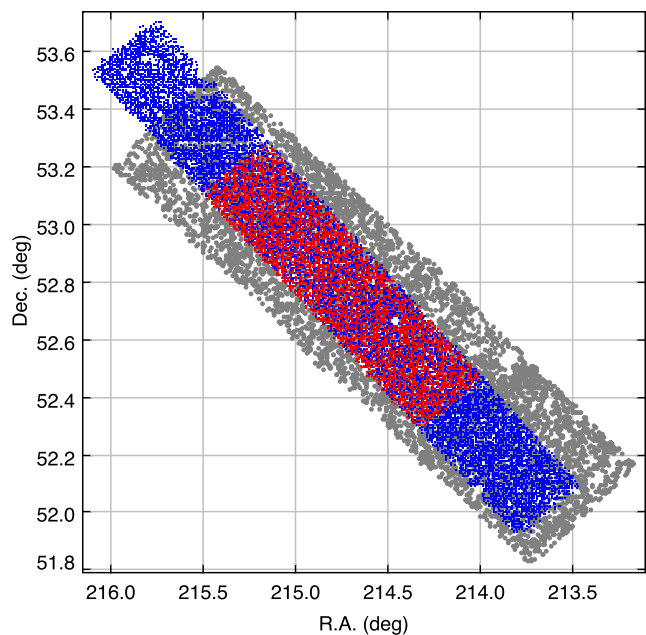
Fig. 3. Footprint of the miniJPAS and DEEP2/DEEP3 spectroscopic observations. Grey circles represent miniJPAS sources with $r<23$, while blue and red dots represent sources targeted for spectroscopy by the DEEP2 and DEEP3 surveys, respectively.

samples. Any determination of statistical properties of miniJPAS galaxies based on such partitioning, (including the redshift distribution) would be biased at faint magnitudes.

To solve this issue, we compute photo-z for all miniJPAS sources regardless of the morphological classification. For each source we obtain $P(z|G)$, the redshift probability distribution conditional to the source being a galaxy, which depends on its SED alone. If a source is known to be a star or quasar ($P_S = 1$) then the value of $P(z|G)$ is meaningless. However, by computing $P(z|G)$ independently of any morphological information and applying the morphological classification as a posterior, we can easily estimate redshift-dependent statistics for the population of miniJPAS galaxies that account for the uncertainty in the classification of individual sources (see Sect. 6).

2.5. Spectroscopic redshifts

The Deep Extragalactic Evolutionary Probe 2 (DEEP2) and 3 (DEEP3) galaxy redshift surveys (Davis et al. 2003; Cooper et al. 2011; Newman et al. 2013) cover about half of the area of the miniJPAS survey (Fig. 3). Both surveys were performed with the DEIMOS multi-object spectrograph on the Keck II telescope. DEEP2 spectra were obtained with the 1200 lines/mm grating, covering the ~6500–9100 Å range with a spectral resolution of $R\sim5000$, while DEEP3 used the 600 lines/mm grating, allowing for a wider spectral coverage (~4550–9900 Å) at $R\sim2500$.

We retrieved the combined DEEP2/3 redshift catalogue for the EGS[2], which contains a total of 23822 unique sources. Targets for DEEP2 observations were selected at random from the $R<24.1$ flux limited catalogue of Coil et al. (2004), which covers the entirety of the EGS. By contrast, DEEP3 covers only the central part of the EGS. While most DEEP3 targets are also selected

---

[2] http://deep.ps.uci.edu/deep3/zcat_archive/
alldeep.egs.uniq.2012jun13.fits.gz
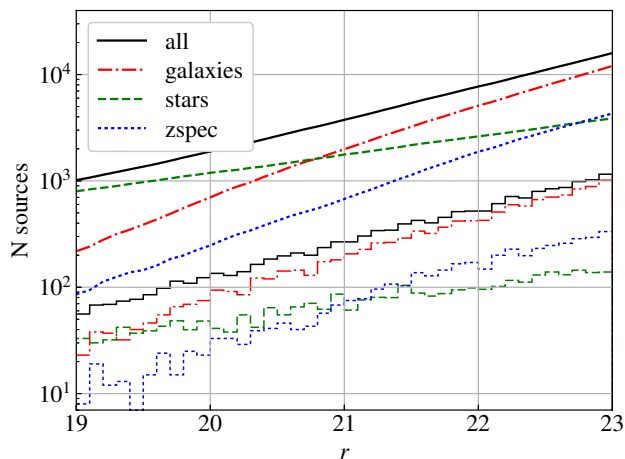
Fig. 4. Distribution of miniJPAS sources as a function of *r*-band magnitude for all sources (black solid lines), stars (green dashed lines), galaxies (red dot-dashed lines), and galaxies with spectroscopic redshifts (blue dotted lines). Smooth lines show cumulative counts while histograms show counts in bins of 0.1 magnitudes.

from the *R*<24.1 sample, additional sources were targeted based on detection at other wavelengths, such as far-infrared or X-rays, including some *R*>24.1 sources. We remove these sources from the catalogue to keep the spectroscopic sample representative of the population of *R*<24.1 sources. We also require that sources have secure redshifts (ZQUALITY >=3) and spectral classification as galaxy. There are 15,222 sources meeting all these criteria.

We perform a match by coordinates between this sample and the miniJPAS catalogue using a search radius of 1.5". We find spectroscopic counterparts for 4,825 out of 20,962 miniJPAS sources brighter than *r*=23, at an average matching distance of 0.12".

We also match the miniJPAS catalogue with the spectroscopic redshift catalogue from SDSS DR12, which covers the entirety of the miniJPAS footprint. Again, we keep only matches for sources with secure spectroscopic redshifts (zwarning = 0) and spectroscopic classification as galaxy. 564 sources meet these criteria, including 123 that also have redshifts from DEEP. In all the galaxies in common between SDSS and DEEP their redshift measurements agree to within $|\delta z|<0.001$, the median $|\delta z|$ being 0.00012.

Figure 4 shows the distribution of sources of all types, galaxies, and galaxies with spectroscopic redshifts as a function of the *r*-band magnitude in the miniJPAS catalogue. The distribution for all sources is computed without taking into account the morphological classification and is dominated by stars at *r*<19.5. The distributions for stars and galaxies are obtained by weighting each source with its P_S and P_G, respectively. Finally, the distribution for galaxies with spectroscopic redshifts is computed from the subsample with matches in our spectroscopic catalogue.

The fraction of miniJPAS galaxies with spectroscopic redshifts is roughly constant at ~25% within the range 19< *r* <23. This fraction increases to ~50% if we consider only sources within the DEEP footprint (the number of SDSS spectra for *r*>19 galaxies is negligible).
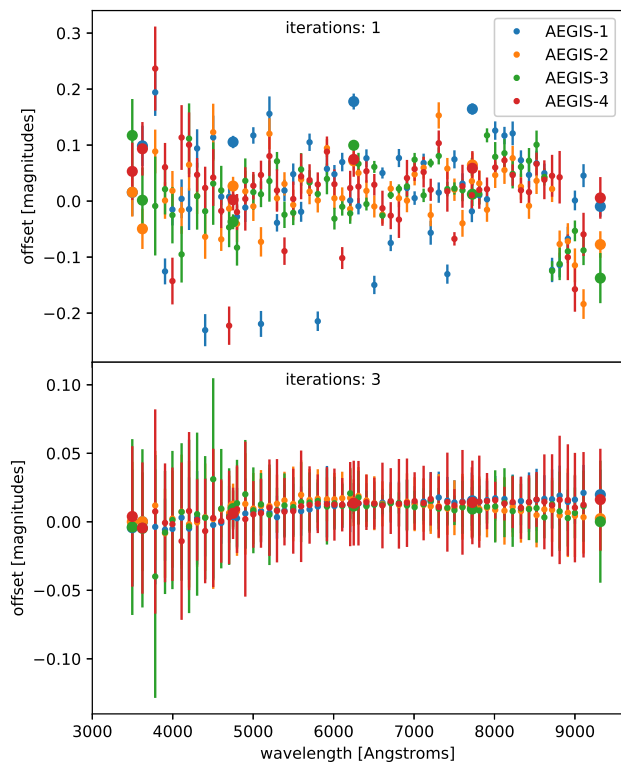
Fig. 5. Magnitude residuals between the observed and synthetic photometry after the first (top) and third (bottom) iterations of the recalibration procedure. Symbols indicate the median residual while error bars enclose the 16th to 84th percentile ranges. Small symbols correspond to photometry the narrow-band J-PAS filters while large ones represent broadband filters (uJAVA, uSDSS, gSDSS, rSDSS, iSDSS) and the long-pass J1007 filter.

3. Recalibration

The observed colours of galaxies may be affected by systematics in the photometry originating from errors in the absolute flux calibration of the images, in the correction for Galactic extinction, or aperture effects introduced by PSF variation among images in different bands. Because accurate galaxy colours are essential for photometric redshifts, many SED-fitting photo-z codes include a pre-processing stage dedicated to computing magnitude offsets for each band that minimise the average colour differences between the observed photometry and synthetic photometry extracted from the spectral templates (e.g. Ilbert et al. 2006; Molino et al. 2014; Eriksen et al. 2019). We call this process zero-point recalibration, or recalibration for short. Since the spectral templates are also affected by calibration uncertainties, this procedure has the advantage of putting the observed photometry and the templates in the same "photometric system".

A major shortcoming of this approach is that the template set usually contains only a few "archetype" templates representative of the broad spectral types expected to be found in the sample. For datasets such as miniJPAS, with observations in many bands, this implies that poor fits (high χ^2 values) are obtained for many sources (in particular the ones with highest S/N) even after the recalibration offsets have converged, because the template set is not big and diverse enough to reproduce all the variety of spectral features found in individual galaxies. Discrepancies between the best-fitting template and the actual spectrum of the galaxy increase the dispersion in the magnitude offsets calculated from

different galaxies for each band, implying a more uncertain correction.

To overcome this issue, we instruct the photo-z code to skip the recalibration step[3] and instead we perform the recalibration separately, using a custom routine. This allows us to use a very large grid of spectral templates, built from stellar population synthesis models, which can reproduce the SED of miniJPAS galaxies to much higher accuracy.

3.1. Grid of models

We generate a grid of 90,720 synthetic spectra with the python implementation of CIGALE, that is described in Boquien et al. (2019). Each one represents the theoretical spectrum of a galaxy composed of two stellar populations (namely 'young' and 'old'). The old population is assumed to have a delayed-exponential star formation history (SFH), with age between 2 and 10 Gyr and e-folding timescale between 0.5 and 2 Gyr. The SFH for the young population is also a delayed-exponential, with age between 0.1 and 1 Gyr and e-folding timescale between 50 and 200 Myr. The fractional contribution of the young population to the total stellar mass of the galaxy may take values from 0% to 10%.

The synthetic spectrum for each population is generated by integration over time of a library of simple stellar populations (SSPs). We choose the high spectral resolution version of the library of Bruzual & Charlot (2003), with a Chabrier (2003) initial mass function (IMF), and stellar metallicities $Z/Z_\odot$ = 0.2, 0.4, and 1.0. The nebular emission is modelled with the grid of nebular templates from Inoue (2011), which were generated using CLOUDY 13.01 (Ferland et al. 1998, 2013). The metallicity of the gas is assumed to be the same as that of the stellar component. To keep the total number of models manageable, we restrict values of the ionisation parameter to the range log U = [-3,-1] in steps of 0.5. The fraction of Lyman continuum photons reprocessed into nebular emission (that is, not absorbed by dust or escaping into the intergalactic medium) ranges from 5% to 100%. The attenuation law is Calzetti et al. (2000), and the colour excess E(B-V) of both stellar components is fixed at 0.44 times that of the nebular component (which takes values from 0 to 0.5 mag in steps of 0.1).

3.2. Computation of offsets

We perform the recalibration using miniJPAS galaxies with secure spectroscopic redshifts and spectroscopic classification as "galaxy" from either SDSS or DEEP. Since complete and accurate SEDs are essential for the recalibration procedure, we exclude sources fainter than r=22 or with flags in the photometry of any of the 60 bands.

We obtain recalibration offsets independently for each of the four pointings of the miniJPAS survey using ~500 galaxies per pointing. For each galaxy, the model rest-frame spectra in the grid are redshifted to the observed frame of the galaxy. Then synthetic photometry is obtained by convolving the redshifted spectra with the transmission curves of the filters, and a scaling factor is found that provides the best fit (minimum χ^2) between the observed and synthetic SEDs. We select as the best model for each galaxy the one that produces the absolute minimum χ^2 among the 90,720 models in the grid. Then, for every pointing,

we compute the systematic offset in the photometry for band j as:

$$\delta m(j) = \text{median}\{m_i^{obs}(j) - m_i^{synth}(j)\} \quad (2)$$

where $m_i^{obs}(j)$ and $m_i^{synth}(j)$ are, respectively, the observed and synthetic magnitudes in band j for the i-th galaxy. The observed photometry is adjusted by subtracting the offsets just computed:

$$m_i^{corr}(j) = m_i^{obs}(j) - \delta m(j) \quad (3)$$

We repeat the SED-fitting with the grid of models for the updated photometry and recompute the offsets iteratively, until all new additional offsets are smaller than 0.001 magnitudes, which in practice happens after 3 or 4 iterations (Fig. 5). The cumulative offsets resulting from the addition of the successive offsets in all the iterations, $\Delta m(j) = \delta m(j) + \delta m'(j) + \ldots + \delta m^n(j)$, are the final recalibration corrections, which we apply to the original photometry for all the sources in the pointing.

We estimate the uncertainty in the recalibration offsets as the uncertainty in the median of the residuals after the last iteration, assuming a normal distribution:

$$\sigma(\Delta m(j)) = \sqrt{\frac{\pi}{2N}}\sigma\{m_i^{obs}(j) - \Delta m(j) - m_i^{synth}(j)\} \quad (4)$$

where N is the number of galaxies used and $m_i^{obs}(j)$ - $\Delta m(j)$ is the magnitude in band j of the i-th galaxy after recalibration.

The recalibration offset computed for a given band differs significantly from one pointing to another, mostly due to differences in the PSF FWHM of the images. Table 3 indicates the offsets and their uncertainties for PSFCOR magnitudes in the 60 bands for the the four miniJPAS pointings.
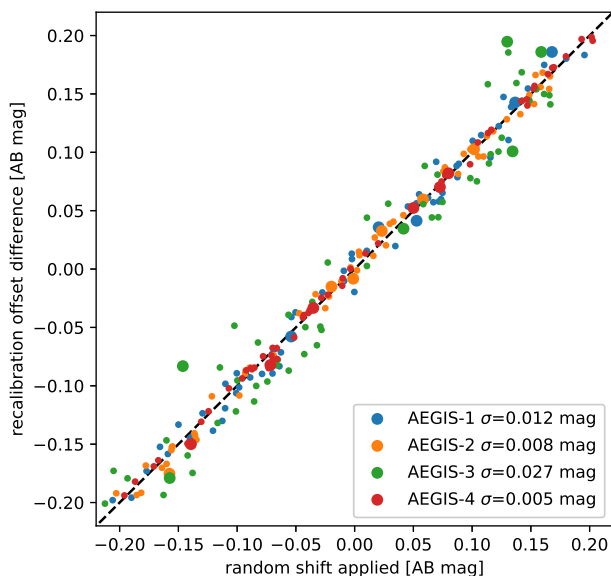
3.3. Validation of recalibration offsets

The recalibration procedure may raise some legitimate concerns about its robustness. One possible source of problems is degeneracy between offsets caused by systematic errors in the photometry and those in the spectral templates. If most of the galaxies in the recalibration sample are within a small redshift range, any given spectral feature will appear most of the time in only a few bands. This has the potential of biasing the recalibration if the best-fitting models for these galaxies systematically under- or over-predict the intensity of the feature. Emission lines, whose intensity is particularly hard to predict from the observed continuum, are one clear example.

In order to check whether this degeneracy is an issue for the miniJPAS sample, we split the recalibration sample for each pointing into two subsamples, one containing all the galaxies with redshift below the median of the sample and the other with the ones above. We perform the recalibration separately for the two subsamples and compare the resulting offsets. We find that the offsets calculated for the two subsamples are consistent within their uncertainties.

Another sensible concern is the unicity of the results from the recalibration procedure. To test whether the recalibration converges to the same corrected photometry irrespective of the systematic offsets, we modify the observed photometry by applying random shifts between -0.2 and +0.2 magnitudes (selected from an uniform distribution). The same shift $x(j)$ is applied to all galaxies for each band j to simulate a systematic offset.

---

[3] in LePhare this is done by setting AUTO_ADAPT=NO in the configuration file

Fig. 6. Comparison between the arbitrary shifts introduced in the input photometry for individual bands (X axis) and the resulting change in the recalibration offsets obtained (Y axis). Symbols as in Fig. 5. The dashed line marks the 1:1 relation expected when the recalibration process compensates perfectly systematic offsets in the photometry.

We compute recalibration corrections, $\Delta m^*(j)$, for this modified photometry using the exact same method as before. If the recalibration can compensate for these additional systematic shifts, then we expect the difference between the original and the new recalibration offsets to match the shift applied to the photometry:

$$\Delta m(j) - \Delta m^*(j) \approx x(j) \tag{5}$$

Figure 6 compares the random shifts introduced, $x(j)$, with the resulting change in the recalibration offsets, $\Delta m(j)$-$\Delta m^*(j)$, for all the bands and pointings. The dispersion around the 1:1 relation is ~0.01 mag (except for pointing AEGIS-3, which has σ~0.03 mag), an order of magnitude smaller than the shifts introduced and also comparable or smaller than the uncertainties calculated for the original recalibration offsets (see Table 3).

This suggests that the recalibration procedure converges to the same or very similar stellar population models for most galaxies, regardless of any systematic shifts in the photometry. Therefore, we conclude that the offsets $\Delta m(j)$ obtained in the recalibration remove real systematics in the photometry, probably associated to imperfect aperture corrections.

We emphasise that the $\Delta m(j)$ in Table 3 are valid only for the PSFCOR aperture. Also, we warn the reader about the systematic errors that could be introduced if these recalibration offsets are used in the spectral analysis of miniJPAS sources. Their values may still be model-dependent with regards to the specific choice of the stellar library, the extinction law, or other model parameters. However, this is not a problem for our photo-z calculation since the template library that we use is a subset of the model grid (see Sect. 4.2).

4. Computation of photometric redshifts

4.1. Photo-z code

We compute photo-z for miniJPAS sources using JPHOTOZ, a python package that is part of JYPE, the data reduction pipeline for J-PAS. JPHOTOZ acts as an interface between the database and the actual photo-z computing code(s) and also handles all the pre- and post-processing of the data, including: application of Galactic extinction correction and recalibration offsets to the photometry, filtering of flagged photometric measurements, contrast-correction of the redshift probability distribution function (zPDF; see Sect. 4.3), and computation of the *odds* parameter as well as other parameters derived from the zPDF (Sect. 4.4).

The photo-z code used for miniJPAS is a customised version of LePhare (Arnouts, & Ilbert 2011), modified to remove a limitation in the maximum number of bands in the photometric catalogue (32 in the original LePhare), as well as to allow for higher resolution in redshift with a finer sampling of the redshift search range (in miniJPAS, from z=0 to z=1.5 in constant steps of δz=0.002). LePhare computes photo-z using the template-fitting method (see Salvato et al. 2019, for a recent review of the different photo-z techniques). Template fitting photo-z works by evaluating a goodness-of-fit estimator (typically χ^2) between the observed photometry and synthetic photometry generated from each of the templates as a function of z. The corresponding χ^2 values sample the (assumed Gaussian) log-likelihood distribution, $\log \mathcal{L}(z) \propto -\chi^2_{min}(z)/2$. Most modern photo-$z$ codes (including LePhare) compute the zPDF by weighting $\mathcal{L}(z)$ with a redshift prior that summarises our *a priori* knowledge of the underlying redshift distribution as a function of the galaxy magnitude and/or colour (see Ilbert et al. (2006) for details and Benítez (2000) for a general description of the method).

We use the default redshift prior in LePhare, which is obtained from the spectroscopic redshift distribution of galaxies in the VIMOS VLT Deep Survey (VVDS; Le Fèvre et al. 2005), and contains the probability density function $P(z,T|m)$ of the redshift and spectral type as a function of the i-band magnitude. Figure 7 shows $P(z,T|m)$ for the broad spectral types "elliptical" (E/S0), "spiral" (Sp), and "irregular" (Irr), defined according to the rest-frame $g-i$ colour of the templates (see Ilbert et al. (2006) for details), and for magnitudes i=21, 22, and 23. For galaxies brighter than $i = 20$ the empirical prior is replaced by a step function that takes the value 1 at $z \leq 1$ and 0 at $z>1$, independently on the spectral type. While such a prior is not a realistic model for the actual redshift distribution of bright galaxies, this fact is unimportant in practice since $i<20$ miniJPAS galaxies have high S/N photometry and their $\log \mathcal{L}(z)$ present a very sharp peak. The prior also prevents $i<20$ sources from finding solutions at $z>1$. This is not an issue for miniJPAS given its small volume (the brightest galaxy with $z_{spec}>1$ has i=20.6), but a more realistic prior will be needed for J-PAS in order to obtain accurate photo-z for the most luminous $z>1$ galaxies.

LePhare also calculates separately the minimum χ^2 obtained with a set of stellar and quasar templates, which could help to classify sources. However, we find it more convenient to exclude such templates and to interpret the zPDF from LePhare as the redshift probability distribution conditional to the source being a galaxy, $P(z|G)$.
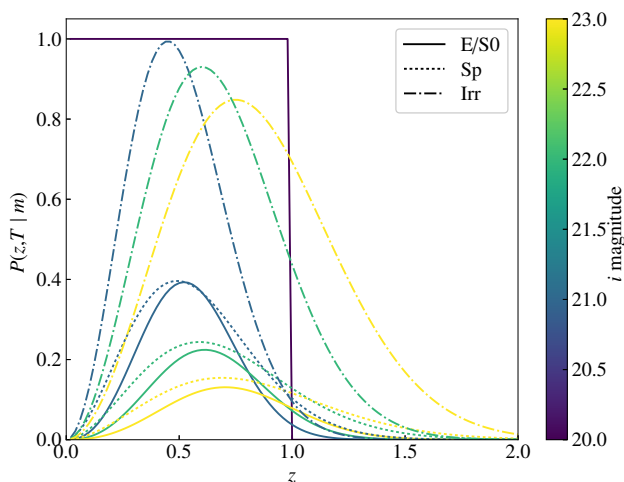
Fig. 7. Prior probability redshift distributions used by LePhare, for the broad spectral types "elliptical" (solid line), "spiral" (dotted line), and "irregular" (dot-dashed line), with colour coding for the magnitude (see text for details).

4.2. cefca_minijpas *library of templates*

A key aspect of the template-fitting method for photo-z determination is that generally it does not require a good fit between the template and the observed photometry; it suffices that the best fit is obtained at the true redshift. In particular, only a few templates (broadly corresponding to the major spectral types) are needed to obtain good photo-z from broadband photometry (e.g. Benítez 2000), where photo-z accuracy depends on the correct detection of broad spectral features like the Lyman break or the 4000 Å break.

The requirements are different when using narrow-band photo-spectra, since narrow spectral features such as emission and absorption lines have a much stronger impact on the photometry (the effect of a spectral feature on the photometry is proportional to its equivalent width and inversely proportional to the bandpass). Multiple works have shown that photo-z for narrow-band datasets improve significantly when emission lines are taken into account (e.g. Molino et al. 2014; Eriksen et al. 2019; Alarcon et al. 2021)

LePhare can add emission lines to the templates with intensities individually adjusted for each galaxy to match the photometry in the affected bands. However, this often results in too much freedom, as it allows unphysical models that lead to spurious solutions. Because of this, we prefer to switch off the emission line adjustment capability in LePhare and instead provide templates that include both the stellar and nebular emission (lines and continuum).

In the past, template libraries were conditioned by the availability of spectral templates, which were often based on the observed spectra of archetypal galaxies or composites from multiple galaxies of the same type, often extrapolated with models or photometry beyond the range of the spectroscopic observations. An alternative approach that has gained popularity thanks to improvements in the stellar libraries and stellar evolution models is the generation of synthetic galaxy spectra with SPS models (e.g. Brammer et al. 2008; Eriksen et al. 2019).

To build the cefca_minijpas library of templates we start from the grid of 90,720 SPS models that we used for the recalibration. Because we want to use templates that represent real galaxies,
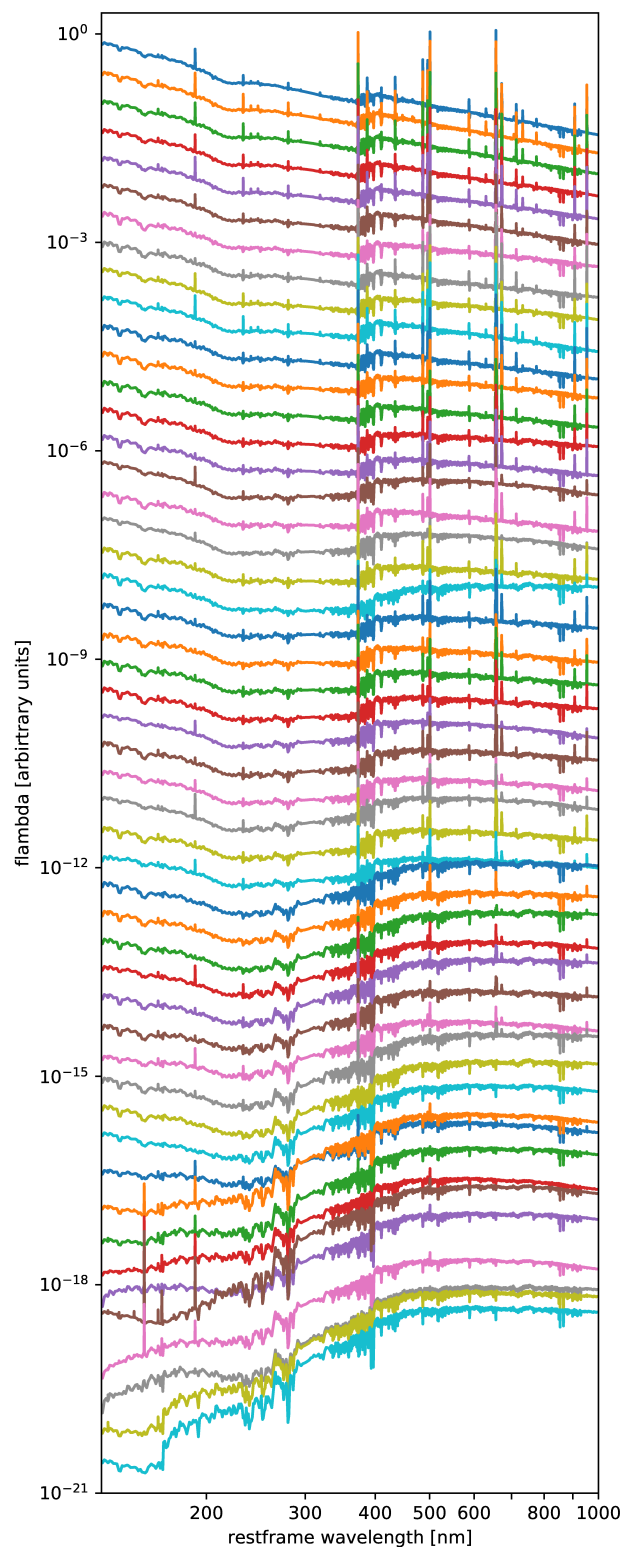
Fig. 8. The 50 galaxy templates used for computation of photo-z for miniJPAS sources, sorted by their rest-frame UV-to-optical spectral index and shifted in the Y axis for clarity.

we choose only those that provide the best fit for one (or more) of the miniJPAS galaxies using the recalibrated PSFCOR photometry. We exclude sources fainter than $r = 22$ to guarantee a good S/N in all the bands, and also consider only sources with secure spectroscopic redshifts. We make sure that the best-fitting

template is consistent with the observed photometry by requiring a reduced chi-squared $\chi_r^2 < 1$. We also impose a constraint on the coefficient of variation of the RMS error:

$$CV_{\mathrm{RMSE}} = \frac{\sqrt{\sum_{n=1}^{N} \left(f_{obs}(\lambda_n) - f_{model}(\lambda_n)\right)^2 / N}}{\sum_{n=1}^{N} f_{obs}(\lambda_n) / N} \qquad (6)$$

which represents the ratio of the typical residual to the mean flux. We require $CV_{\mathrm{RMSE}} < 0.04$ because selecting for low χ_r^2 alone favours the sources with lower S/N (see e.g. Hernán-Caballero et al. 2015), for which a wider range of models is consistent with the observed photometry. There are 455 SPS models meeting all these criteria.

We further reduce the number of templates by iteratively performing photo-z calculation with multiple combinations of these 455 models to select the ones that provide the best results in the spectroscopic subsample. This method for optimisation of the template set is the subject of an upcoming paper (Hernán-Caballero et al., in preparation). Very briefly, a score is associated to each combination of templates, which summarises the quality of the photo-z obtained on a test sample with those templates. Starting from random selections of templates, each set of templates is modified by removing some and adding new ones at random (selected from the population of 455 candidates). The score is computed for every new set. Then, those with higher score are taken as the basis for new sets with higher probability. We iterate until the best score among all the sets maxes out and no further increases are obtained in a predetermined number of iterations. We take the set with the highest score as the final selection, and use it to compute the photo-z for the whole miniJPAS sample.

We repeated this procedure multiple times with different random initial sets. While the final selection changes from one run to another, the score converges to the same maximum value in all the runs, and the photo-z of the whole miniJPAS sample in two different runs are identical for ~98% of the sources. Some particular templates always get into the final selection, others seem interchangeable, and the large majority never gets selected.

The final set used to compute the published photo-z of miniJPAS contains 50 templates (number for which the precision saturates) and is shown in Fig. 8. The values of the main parameters used to build these models are listed in Table 4 and common observables measured on the models are presented in Table 5.

4.3. Contrast correction of the zPDF

The probabilistic nature of the zPDF implies that for individual sources, it is often impossible to tell whether they are realistic or not, as any $P(z|G)$ that verifies $P(z_{\mathrm{spec}}|G)>0$ is consistent with the spectroscopic redshift. However, when considering large groups of sources, some statistical tests can determine if the zPDF are well behaved. One powerful test is the calculation of the fraction of galaxies in which z_{spec} falls within a given confidence interval (CI) of the zPDF (e.g. Fernández-Soto et al. 2002; Dahlen et at. 2013; Schmidt & Thorman 2013). If the zPDF describes the actual redshift probability distribution, we can expect 10% of galaxies to fall within any 10% CI, 20% in a 20% CI, and so on. Out of the many possible definitions of a CI, the most useful is the highest probability density (HPD) CI, as proposed initially by Fernández-Soto et al. (2002) and illustrated by Wittman et al. (2016). The HPD CI is the shortest redshift interval (or union of disjoint intervals) that contains a given fraction
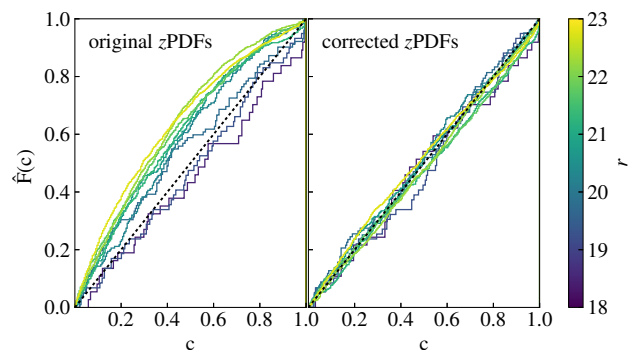
Fig. 9. Fraction of galaxies with z_{spec} within the highest probability density confidence interval as a function of the confidence level before (left) and after (right) the contrast correction of the zPDF. Galaxies are grouped by their r-band flux in bins of 0.5 magnitudes. The diagonal line marks the $\hat{\mathrm{F}}(c) = c$ relation expected if the zPDF represents the actual redshift uncertainty. Values above (below) this line imply under-(over-)confidence in the z_{best} estimate.

of the total area under the zPDF distribution. Therefore, it always encloses the main peak of the zPDF.

We compute the fraction $\hat{\mathrm{F}}(c)$ of miniJPAS galaxies with z_{spec} inside the HPD CI at confidence level c using the algorithm presented in Wittman et al. (2016). We separate the galaxies into groups according to their r-band magnitude. The results (left panel in Fig. 9) show that, in general, there are more z_{spec} values inside the HPD CI than expected, indicating that the zPDF has too much weight at redshifts far from the main peak (or peaks). This effect is increasingly strong at fainter magnitudes. For bright sources ($r<19$), the opposite is true: too much weight is placed at the main peak of the zPDF, causing $\hat{\mathrm{F}}(c)<c$.

This type of inaccuracies in the zPDF is a common issue of photo-z codes, which causes under- (or over-)estimation of the actual redshift uncertainty (e.g. Hildebrandt et al. 2008; Dahlen et at. 2013; Mundy et al. 2017). Several factors may contribute to these trends, including over- (or under-) estimation of photometric errors and the sparse sampling of the parameter space of the models that results from using only a few templates. The latter implies that the best-fitting template is often substantially different from the actual spectrum of the source. Such sparseness of the models is particularly relevant for miniJPAS, where the high number of narrow-band filters allows to resolve many spectral features. Because of this, most galaxies get poor fits ($\chi_{min}^2 \gg 1$) even at the spectroscopic redshift, in particular those with higher S/N photometry.

Modelling the impact on the zPDF of all the factors described above is overly complex and ultimately unnecessary. An empirical correction of the contrast of the zPDF (the difference between the value at peaks and valleys) suffices to restore the expected relation between $\hat{\mathrm{F}}(c)$ and c. To this aim, JPHOTOZ implements a variation of the method described by Dahlen et at. (2013), which corrects the zPDF in two steps. First, a discrete convolution of the zPDF and a Lorentzian kernel is performed:

$$P'[n] = (P * k)[n] = \sum_{m=-2}^{2} P[n-m]k[n] \qquad (7)$$

where $P[n]$ is the value of the zPDF for the n-th element in which it is sampled (corresponding to the redshift $z[n] = 0.002n$), and

$k[m] = 1/(m^2 + \gamma^2)$, with γ=1.18. This convolution is particularly important for bright sources, that sometimes have $P[n] = 0$ for all elements except the one corresponding to the peak. The contrast of the convolved zPDF is then adjusted with the transformation $P''[n] = P'[n]^{1/\alpha}$, with $\alpha = 0.54$. The values of α and γ are calculated by minimising over the whole sample the function:

$$D(\alpha, \gamma) = \sum_i |\hat{F}(c_i) - c_i| \qquad (8)$$

The right panel in Fig. 9 shows the relation between $\hat{F}(c)$ and c for the same magnitude cuts after the contrast correction.

4.4. Scalar parameters

While the zPDF provides the most complete description of our knowledge of the redshift of a source, it is often more convenient to use scalar parameters that condense its main properties. The table *PhotoZLephare_updated* in the miniJPAS database[4] contains several of them:

- **Z_ML** (Z_ML in LePhare) is the median redshift of the zPDF (50% of the total area is on each side).

- **PHOTOZ** (Z_BEST in LePhare, hereafter z_{best}) is the redshift corresponding to the absolute maximum of the zPDF. We consider this the most useful point estimate of the photo-z, as it is more robust than Z_ML for asymmetric or multi-peaked zPDF profiles.

- **CHI_BEST** (CHI_BEST in LePhare) is the χ^2 of the best-fitting galaxy model at z_{best}.

- **Z_BEST68_LOW** (Z_BEST68_LOW in LePhare) the low-z limit of the 68% confidence interval for z_{best}, computed using the $\Delta\chi^2$ method (e.g. Anvi 1976; Bolzonella et al. 2000).

- **Z_BEST68_HIGH** (Z_BEST68_HIGH in LePhare) the high-z limit of the 68% confidence interval for z_{best}, computed using the $\Delta\chi^2$ method.

- **PHOTOZ_ERR** is the 1-σ uncertainty in z_{best}, computed as: PHOTOZ_ERR = 0.5(Z_BEST68_HIGH - Z_BEST68_LOW). In this paper we use a related quantity, the relative 1-σ uncertainty:

$$z_{err} = \frac{\text{Z\_BEST68\_HIGH} - \text{Z\_BEST68\_LOW}}{2(1 + \text{Z\_BEST})} \qquad (9)$$

- **ODDS** (hereafter *odds*) is the probability of the relative error in z_{best} being smaller than 3% ($|\Delta z| = |z_{best} - z_{spec}|)/(1+z_{spec})<0.03$). Unlike all the others, this is not a direct output from LePhare, but is computed by jphotoz from the contrast-corrected zPDF, using the formula:

$$odds = \int_{z_{best}-d}^{z_{best}+d} P(z|\text{G})dz, \qquad d = 0.03(1 + z_{best}) \qquad (10)$$

---

[4] http://archive.cefca.es/catalogues/minijpas-pdr201912

5. Quantifying the photo-z accuracy

5.1. Origin of errors in photo-z

Taking the spectroscopic value as the true redshift of the galaxy, the error in z_{best} is often defined as: $\Delta z = (z_{best} - z_{spec})/(1 + z_{spec})$, where the $1+z_{spec}$ factor conveniently compensates for the stretching of spectral features with redshift. The value of Δz is determined by two main types of error, which differ substantially in their prevalence and impact on the resulting photo-z. Broadly speaking, we can describe them as "inaccuracies" and "catastrophic errors".

The former are the cumulative effect of small systematic and random errors in the photometry, flux calibration, and wavelength calibration, as well as the uncertainty introduced by the limited spectral resolution of the photo-spectra, the finite number of templates, and the discretisation of the redshift search range, to name a few. Each of these factors influences the shape and peak redshift of the zPDF. Combined, they result in a small, largely random shift in z_{best} relative to the true redshift of the galaxy.

On the other hand, catastrophic errors are mainly caused by the non-linearity of the transformation between colour space and redshift, which implies that galaxies with very different spectral types and redshifts may have similar observed colours. The importance of this degeneracy increases at faint magnitudes because larger photometric errors imply more uncertain observed colours which can be consistent with more combinations of template and redshift. The result is a zPDF with two or more peaks of comparable strength at different redshifts, often far apart. When the strongest peak is not the one corresponding to the actual redshift, Δz can be an order of magnitude or more larger than typical inaccuracies. The use of redshift priors mitigates this issue, at least in the aggregate, by favouring the most likely redshift given the magnitude of the galaxy. However, for some galaxies with unusually high or low luminosity, the prior may exacerbate the risk of a catastrophic error by favouring the wrong redshift solution (see Sect. 6.5).

Another cause for catastrophic errors is large errors in the photometry that are not accounted for by the nominal flux uncertainties, such as, in contamination by nearby sources or artefacts in the images which may drastically alter the photometry in one or more bands. The result is often spikes or jumps in the photospectra that the photo-z code tries to match to legitimate spectral features. Fortunately, in the case of miniJPAS the photometry flags identify most of these sources, and the affected bands are masked for photo-z computation. However, a small number of galaxies is likely to be affected by yet undetected issues. Finally, galaxies with "exotic" spectra that do not resemble any of the galaxy templates in the library may also get wrong redshift estimates.

Figure 10 shows the distribution of $|\Delta z|$ for the miniJPAS galaxies with r<23 and with spectroscopic redshifts. The binning is uniform in log $|\Delta z|$ to highlight the bimodality of the distribution caused by the two types of error. The main peak at $|\Delta z|\sim0.004$ corresponds to the typical error due to inaccuracies, while the peak at $|\Delta z|\sim0.04$ represents the catastrophic errors. The first peak and the tail at very small $|\Delta z|$ are well reproduced by a Gaussian or a Lorentzian distribution. The second peak requires a Lorentzian, since the slope of the Gaussian at large $|\Delta z|$ is too steep. Also, the combination of two Lorentzians fits the distribution of $|\Delta z|$ slightly better than the combination Gaussian+Lorentzian.

As we will see in the next sections, the relative importance of inaccuracies and catastrophic errors in shaping the distribution
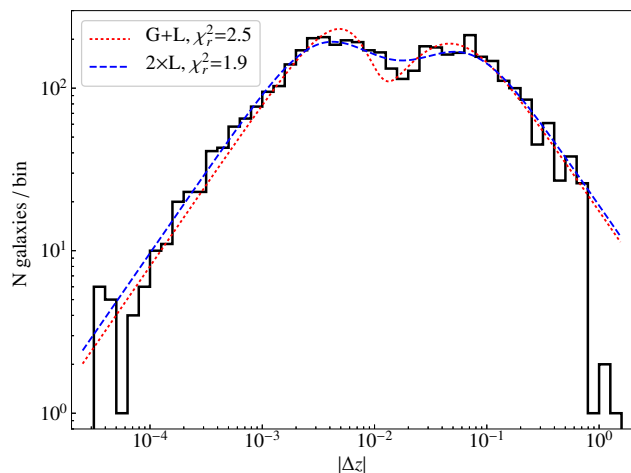
Fig. 10. Distribution of redshift errors for the spectroscopic subsample of miniJPAS (histogram) and best-fitting model combining one Gaussian and one Lorentzian profile (dotted line) or two Lorentzians (dashed line).

Fig. 11. Distribution of the most likely redshift (z_{best}) for all miniJPAS sources brighter than $r=23$ (black solid line), as well as for galaxies (red dot-dashed line), stars (green dashed line), and galaxies with spectroscopic redshifts (blue dotted line).

of Δz varies with properties of the galaxies such as the brightness and redshift, and can be predicted (to some extent) from parameters derived from the zPDF such as z_{err} and *odds*.

5.2. Summary statistics

Similarly to the scalar parameters derived from the zPDF, it is often very convenient to rely on summary statistics of the distribution of Δz in the analysis of the dependence of photo-z accuracy with one or more galaxy properties, or for easy comparison between samples. Since, in most cases, the distribution of Δz is far from Gaussian, the mean and standard deviation are often replaced by more "robust" analogs: the median and the normalised median absolute deviation, σ_{NMAD}. The latter is defined as

$$\sigma_{NMAD} = 1.48 \times \text{median}\left|\Delta z_i - \text{median}(\Delta z_i)\right| \quad (11)$$

where the factor 1.48 is used to match the standard deviation for a Gaussian distribution. Like the standard deviation, σ_{NMAD} is insensitive to a systematic offset in z_{best}, but unlike the former, it is also insensitive to the tail of the distribution for large values of $|\Delta z|$.

A complementary statistic to σ_{NMAD} is the outlier rate, η, which represents the fraction of galaxies with redshift errors larger than a given threshold X:

$$\eta = \frac{N(|\Delta z| > X)}{N_{tot}} \quad (12)$$

where X is set at several times the σ_{NMAD} (in our case, we choose $X = 0.03$) to ensure that only values far from the main peak of the distribution are identified as outliers. As a consequence, η is a good approximation for the frequency of catastrophic errors.

While σ_{NMAD} and η are aggregate statistics that describe the redshift errors of samples, not individual galaxies, their values can also help validate uncertainty estimates for individual sources. In particular, if redshift uncertainties obtained with the $\Delta\chi^2$ method are accurate, we can expect $\sigma_{NMAD} \sim \langle z_{err} \rangle$ for a sample of galaxies selected to have similar values of z_{err}. Also,
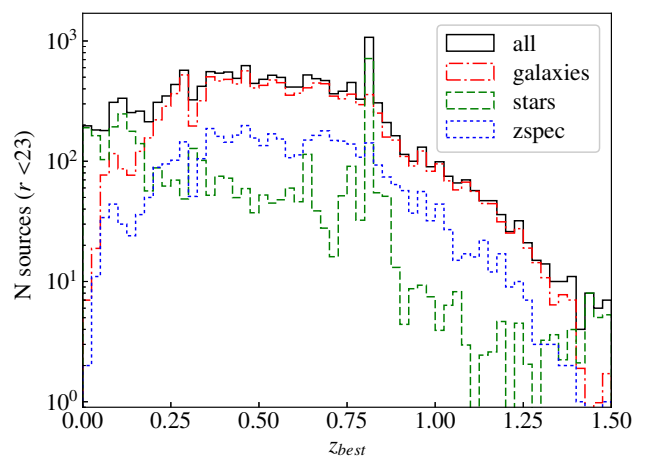
in a sample of galaxies with comparable *odds*, the expected outlier rate is $\eta \sim 1 - \langle odds \rangle$. In Sects. 6.4 and 6.5, we apply these tests to the miniJPAS sample.

6. Results

We compute photo-z for nearly all $r<24$ sources in the dual mode photometric catalogue of miniJPAS. However, we will restrict the analysis to $r<23$ sources, as fainter ones are undetected in most or all of the narrow-band images, and the completeness of miniJPAS for extended sources also drops quickly at $r>23$ (see Fig. 16 in **B21**).

Out of 20,962 miniJPAS sources with $r<23$, 186 (0.9%) were not selected for photo-z calculation due to not meeting the $FLAGS<4$ condition in the selection band (these sources have PHOTOZ = -1 in the redshift catalogue). For another 87 (0.4%) LePhare could not obtain a photo-z measurement due to non-detections in all but one non-flagged bands (PHOTOZ = -99 in the catalogue).

Additionally, we consider as invalid the redshift solutions for all sources where z_{best} is at one of the extremes of the redshift search range ($z_{best} = 0$ or $z_{best} = 1.5$). This is because we cannot determine whether a minimum of $\chi^2(z)$ found at one of the extremes is a local minimum, and anyway the actual number of miniJPAS galaxies at $z=0$ or $z=1.5$ must be very small. Out of 203 sources with $z_{best} = 0$, 200 are clearly stars ($P_S>0.99$) while the remaining 3 are spurious sources in the halo of a bright star. 40 out of 69 sources with $z_{best} = 1.5$ are also point sources, most of them known quasars.

The final number of miniJPAS sources with $r<23$ and valid photo-z is 20,417. Out of these, 15,719 have FLAGS=0 in all bands. In this section we use the later to characterise the photo-z of miniJPAS.

6.1. Redshift distribution of miniJPAS galaxies

Figure 11 shows the distribution of z_{best} for miniJPAS sources brighter than $r<23$. The black histogram is obtained by assigning the same weight $w = 1$ to every source regardless of its morphology, while the green and red ones weight each source by the
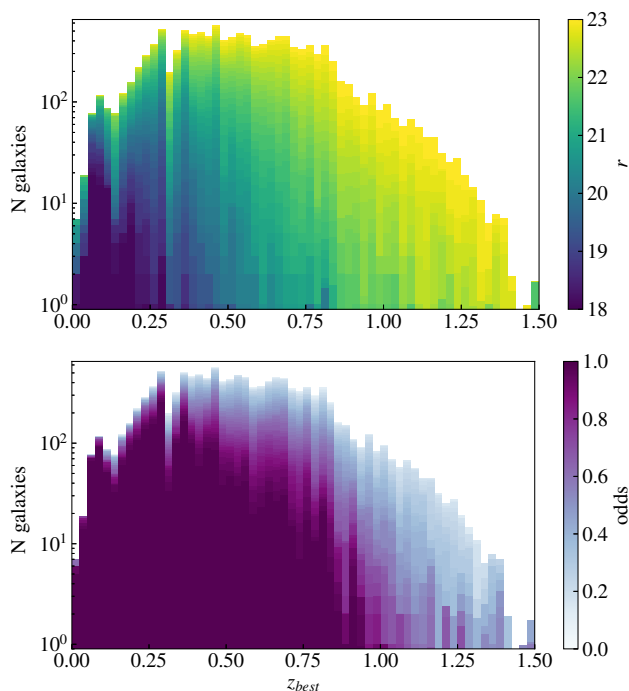
Fig. 12. Redshift distribution of miniJPAS galaxies as a function of the magnitude cut (top panel) or odds cut (bottom panel) applied on the sample.
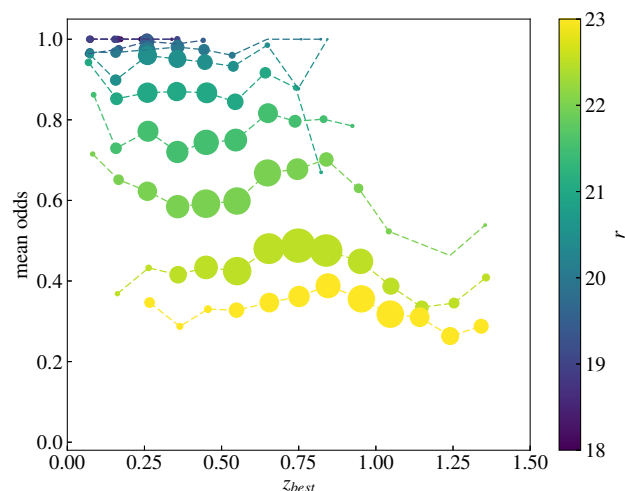

Fig. 13. Mean value of the odds parameter for galaxies as a function of redshift and brightness. Each symbol indicates the average odds for galaxies in bins of width equal to 0.1 in z_{best} and 0.5 in r-band magnitude. Symbol areas are proportional to the effective number of galaxies contributing to each bin.

probability of being a star ($w = P_S$) or a galaxy ($w = P_G = 1 - P_S$), respectively.

While all stars are obviously at $z=0$, their z_{best} estimates span the entire $0<z<1.5$ search range. Stars dominate the number counts at the extremes ($z_{best}<0.2$ and $z_{best}>1.4$) due to a lower number of galaxies detected at these redshifts. There is also a very strong peak at $z_{best}\sim0.82$ that is caused by M-type stars, which find their best fit at that particular redshift. Other weaker peaks in the distribution of z_{best} for stars are also evident in Fig. 11.

Since galaxies represent $\sim80\%$ of the $r<23$ sample, their redshift distribution is very similar to that for all sources, except at both ends of the redshift range where galaxy counts fall steeply. The distribution of z_{best} for galaxies is not smooth, but changes from one redshift bin to the next by more than expected from shot noise. Interestingly, these peaks are mirrored in the distribution of z_{spec}, indicating that miniJPAS can trace overdensities and voids in the radial direction at least up to $z\sim0.8$. It is unclear if structure in z_{best} at $z\gtrsim1$ also corresponds to real over/under-densities, since the spectroscopic counts are too low in this range. In any case, the general trend remains consistent between z_{best} and z_{spec} within the uncertainties up to the photo-z search range limit of $z=1.5$.

The redshift distribution depends strongly on the magnitude of the sources, since higher redshift galaxies are typically fainter. The top panel in Fig. 12 shows the distribution of z_{best} as a function of the limiting r-band magnitude of the selection. Nearly all $z_{best}>1$ galaxies are faint ($r \gtrsim 22$), implying low S/N in the narrow bands. This makes their z_{best} estimates unreliable (low $odds$, see bottom panel in Fig. 12). However, the decrease in the $odds$ at high redshift is steeper than expected from the increase in the average magnitude alone.

Figure 13 shows that at constant magnitude, the mean $odds$ actually increases slightly from $z\sim0.5$ to $z\sim0.8$ but decreases

abruptly at $z>0.8$. This is probably a consequence of the highest contrast spectral features (in particular Hα and the 4000 Å break) shifting into redder bands (where the depth is shallower, see Fig. 4 in B21) and ultimately out of the miniJPAS range.

6.2. Accuracy of z_{best} estimates

In this section, we use the subsample of miniJPAS galaxies with spectroscopic redshifts to evaluate the accuracy of photo-z determinations using the most probable value (the mode of the zPDF), z_{best}. Figure 14 shows the usual comparison between photometric and spectroscopic redshifts. In the case of miniJPAS, a normal scatter plot is not very informative since most of the dots clump in a very narrow band around the diagonal line that marks the 1:1 relation. To give a realistic impression of the actual density of dots along this line, we generate a density map from the scatter plot by convolving with a Gaussian kernel (note that the pixelation and convolution performed to generate the density map cause some broadening of the distribution compared to the original scatter plot).

The dark blue areas indicate the regions with highest density of dots. These correspond to the over-densities found in the distribution of z_{spec} in Fig. 11. The dotted lines enclosing the $|\Delta z| < 0.03$ region contain 64% of the whole $r<23$ sample (left panel) and 87% of the subsample with $odds>0.61$ (right panel).

Comparison of the left and right panels in Fig. 11 shows that most of the dispersion in the z_{best} vs z_{spec} relation is due to galaxies with low $odds$. At faint magnitudes the shape of the zPDF is increasingly dominated by the redshift prior which favours z_{best} values close to the peak probability defined by the prior at each magnitude (see Fig. 7). This implies large errors in z_{best} for sources whose true redshift is far from the $z\sim0.7$ peak of the prior.

The distribution of Δz is noticeably shifted from the origin (Fig. 15), indicating a small positive systematic bias in z_{best}. The shift is evident in all the four AEGIS pointings when considered separately.
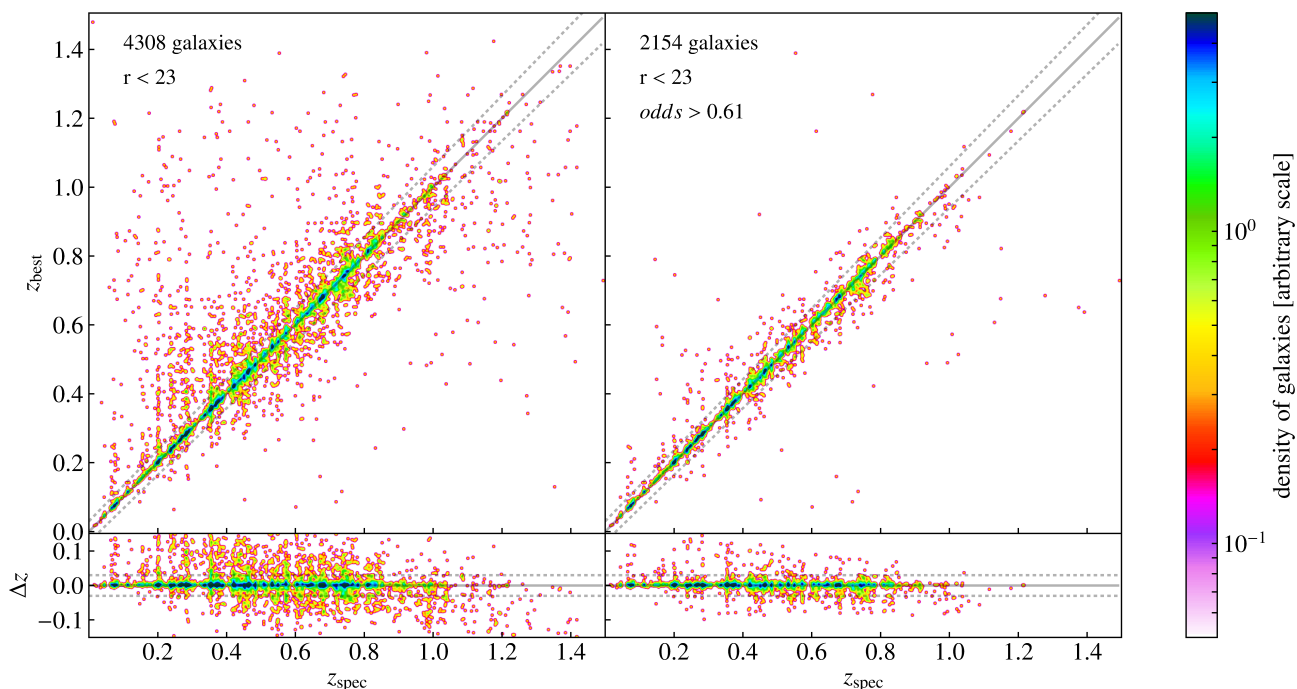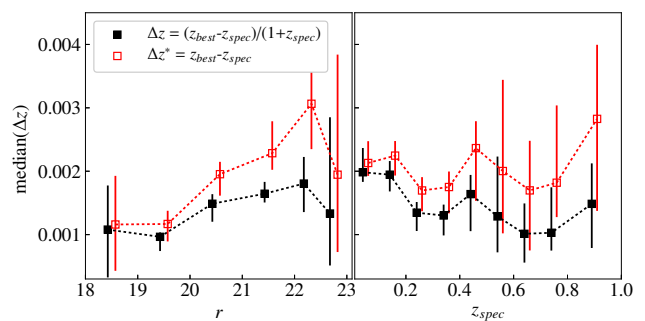
Fig. 14. Comparison between photometric and spectroscopic redshifts for individual miniJPAS galaxies in the spectroscopic sample. The left panel includes all $r<23$ galaxies with valid photo-z estimates while the right one contains only half the sample (those with higher *odds*). The bottom panels show the redshift errors, Δz. A 2-D Gaussian smoothing is applied to the data to improve the visualisation of the density of points. The solid line marks the $z_{\rm best} = z_{\rm spec}$ relation, while the dotted lines indicate the $|\Delta z| = 0.03$ threshold used to define outliers.
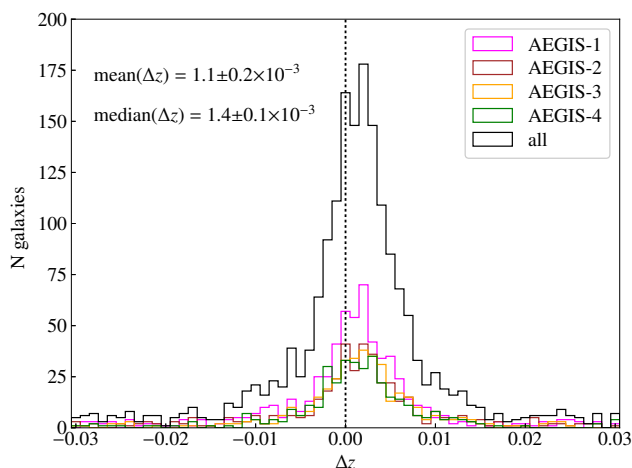
Fig. 15. Distribution of the error in $z_{\rm best}$, Δz, for the galaxies in the spectroscopic sample. The tails of the distribution at $|\Delta z|>0.03$ are truncated to emphasise the shape of the central peak. Only sources with *odds*>0.61 are shown. Each colour represents the distribution for an individual pointing. The black histogram represents the combined distribution for all four pointings.


Fig. 16. Median error in $z_{\rm best}$ as a function of the r-band magnitude (left) and redshift (right) for the galaxies in the spectroscopic sample verifying $|\Delta z|<0.03$ and *odds*>0.65. Solid black symbols and open red symbols represent two different definitions of Δz (see text for details). Error bars indicate the 16–84th percentile confidence interval obtained with bootstrap resampling.

To estimate the magnitude of the systematic bias in $z_{\rm best}$, $\Delta z_{\rm sys}$, we calculate the median Δz among the galaxies with *odds*>0.65 and $|\Delta z|<0.03$. These constraints help to decrease the dispersion introduced by outliers and galaxies with a broad zPDF. We obtain $\Delta z_{\rm sys} = 1.4\pm0.1\times10^{-3}$. The shift is also detected at high significance for other cuts in *odds* or r-band magnitude and for no cuts at all.

We find no dependence of $\Delta z_{\rm sys}$ with the spectral type of the galaxies (see Sect. 6.6 for the details of our classification method). We also check for a dependence of $\Delta z_{\rm sys}$ with the r-band magnitude and redshift of the galaxies in Fig. 16. We find tentative evidence for an increase in the median Δz with r, and a decrease with $z_{\rm spec}$. This is striking, since r and $z_{\rm spec}$ have a positive correlation. The decrease from $\Delta z_{\rm sys}\sim0.002$ at $z\sim0$ to $\Delta z_{\rm sys}\sim0.001$ at $z\sim0.8$ is consistent with a constant offset in $z_{\rm best}$ instead of $z_{\rm best}/(1+z_{\rm spec})$. To prove this, we show in red open symbols the median value of $\Delta z^* = z_{\rm best} - z_{\rm spec}$, which revolves around ~0.002 for the entire redshift range. While an offset of ~0.002 matches the redshift step used in the photo-z calculation and the zPDF, it is unlikely that $\Delta z_{\rm sys}$ is related to the discretisation of the redshift range since we find comparable values for a redshift step of 0.001.
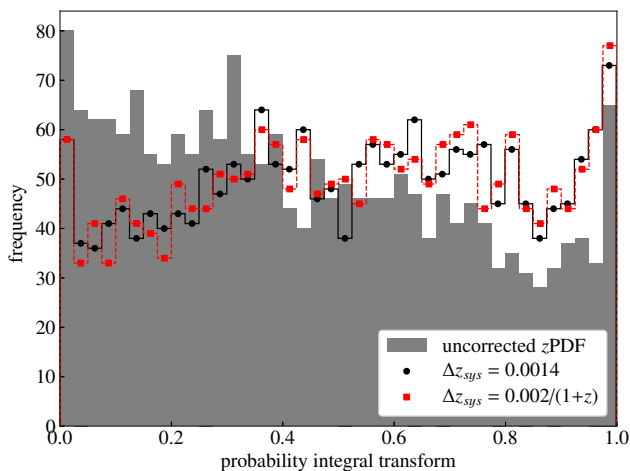
Fig. 17. Distribution of probability integral transform (PIT) values for the *z*PDFs of galaxies in the spectroscopic sample with *odds*>0.65. Black circles and red squares represent the PIT distributions after correcting the individual *z*PDFs assuming a systematic offset of $\Delta z_{sys} \sim 0.0014$ and $\Delta z_{sys} \sim 0.002/(1+z)$, respectively. Grey bars show the PIT distribution with no correction for systematic offset applied.

The systematic bias affects not only the z_{best} values but the entire *z*PDFs, as evidenced by the slope of the distribution of the probability integral transform (PIT) of the *z*PDFs (Fig. 17). PIT values for individual sources are computed as the cumulative distribution function of the *z*PDF evaluated at the spectroscopic redshift (e.g. Schmidt et al. 2020) and represent the probability P($z<z_{\text{spec}}$). Well calibrated *z*PDFs result in a flat distribution of PIT values, while a tilted distribution indicates a bias (Polsterer et al. 2016). Shifting in redshift the *z*PDFs by $\Delta z_{\text{sys}} \sim 0.0014$ or $\Delta z_{\text{sys}} \sim 0.002/(1+z)$ largely removes this bias. The excess frequency in the first and last bins of the PIT distribution are the consequence of catastrophic redshift errors (Schmidt et al. 2020).

The origin of this bias is uncertain. Systematic errors in the wavelength calibration of the JPAS filters is one possibility, as well as errors in the characterisation of the spectral response of the detector or the telescope throughput. However, to produce a shift of $\Delta z_{\text{sys}} = 1.4 \times 10^{-3}$ the effective wavelength of the filters would have to be redshifted by ~9 Å on average, which is more than an order of magnitude larger than the precision of the transmission curves. The same bias could be obtained if the spectral templates are blue-shifted by a similar amount, but this is also highly unlikely as the main emission lines are all found at the expected wavelengths. The redshift prior can, in principle, bias z_{best} values if the width of the prior is comparable to the width of the *z*PDF. However, our redshift prior is flat for *r*<20 galaxies and broad for fainter ones, and the bias is also found for sources with high odds that typically have very narrow *z*PDFs. Finally, the existence of a bug in the code of LePhare is conceivable, but this possibility has been ruled out since roughly the same Δz_{sys} is obtained independently with the TOPz code (Laur et al., in prep.). Because Δz_{sys} is significantly smaller than the nominal uncertainty of most z_{best} estimates and its origin remains unknown, we choose not to correct z_{best} values for this bias.
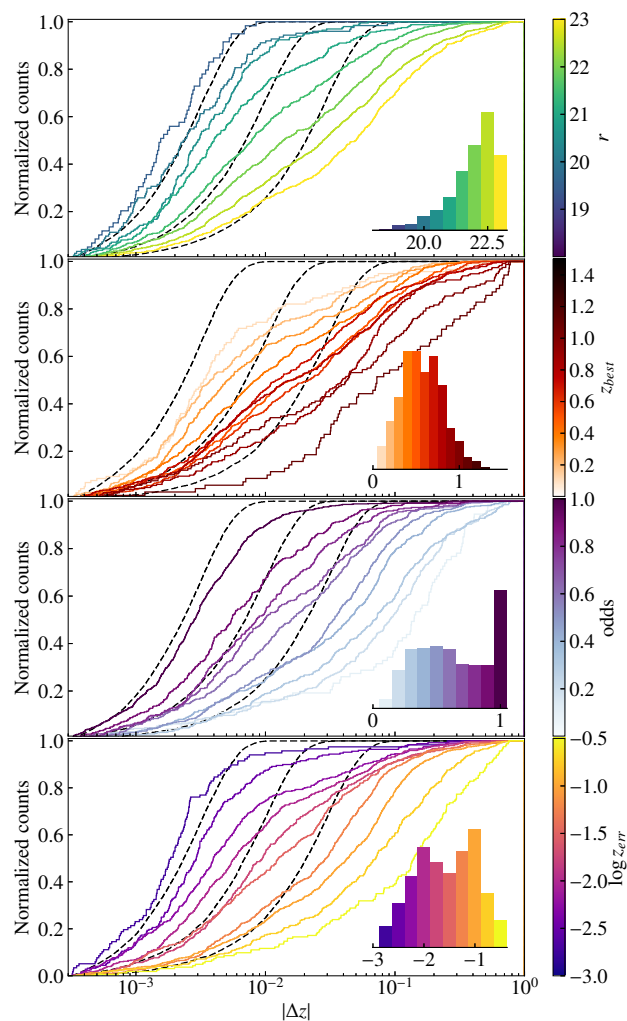
Fig. 18. Cumulative distributions of $|\Delta z|$ for subsets of the spectroscopic sample within specific intervals of (from top to bottom) the *r*-band magnitude, z_{best}, *odds*, and z_{err}. Dashed lines represent predictions for a Gaussian distribution of Δz centred at $\Delta z_{\text{sys}} = 0.001$ and with standard deviations of 0.003, 0.01, and 0.03, while solid lines show the actual distributions for galaxies inside each bin. The inset plots on the right of the panels represent the relative number of galaxies contributing to each bin, coloured according to the central value of the bin. Cumulative distributions for bins containing less than 50 galaxies are not shown.

6.3. Best predictor of photo-*z* accuracy

The distributions of $|\Delta z|$ and Δz shown in Figs. 10 and 15 do not reflect the dependence that photo-*z* accuracy has on many galaxy properties, such as the magnitude of the sources (which determines the S/N of the photometry), the redshift (which conditions the spectral features within the observed spectral range), and the spectral type (which determines the strength of the spectral features). In addition, some parameters derived from the *z*PDF such as z_{err} and *odds* are not real galaxy properties, but clearly depend on them and, in practice, summarise our knowledge about the multiple factors that impact photo-*z* performance. All these quantities correlate, to some extent, with each other and with $|\Delta z|$. In this section, we check how the distribution of errors in z_{best} depends on the *r*-band magnitude, z_{best}, z_{err}, and *odds*, and analyse which quantity is most useful as a predictor of the photo-*z* accuracy for individual sources.
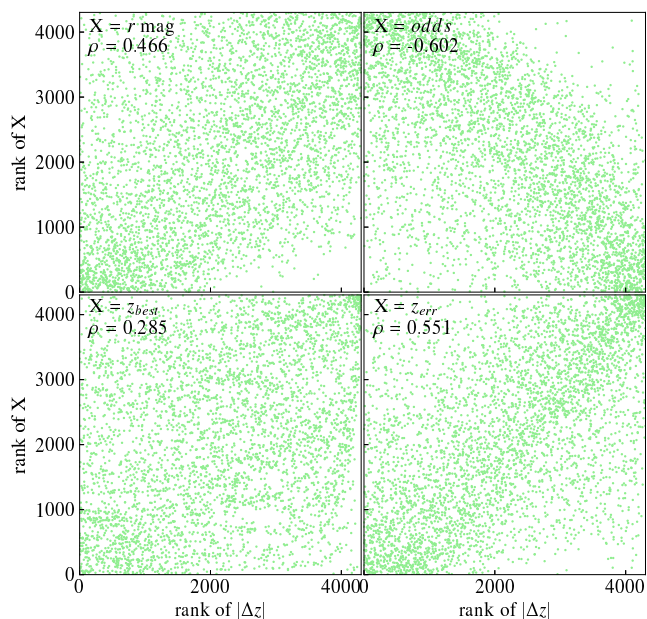
Fig. 19. Comparison of the predictive power for the error in z_{best} of four quantities: the *r*-band magnitude, the value of z_{best}, the *odds* parameter, and z_{err}. Each plot shows the correlation between the ranks of individual galaxies when sorted by each of this quantities and the rank when sorted by $|\Delta z|$. The Spearman rank correlation coefficient (ρ) is quoted for each case.

Figure 18 shows the cumulative distribution of $|\Delta z|$ for subsamples of the spectroscopic sample, selected according to the value of one of these four quantities. We split the range of variation for each of them into same-width intervals. The relative number of galaxies in every interval is shown in the small bar histograms. For reference, we plot in dashed lines the cumulative distributions of $|\Delta z|$ that would result from Gaussian errors with standard deviations of $\sigma(\Delta z) = 0.003, 0.01$, and 0.03.

All four quantities present the same general trend: in the most favourable cases (left-most lines, corresponding respectively to bright *r*-band magnitude, low *z*, high *odds*, or low z_{err}), the distributions of $|\Delta z|$ are nearly Gaussian, with departure from Gaussianity only at the high $|\Delta z|$ tail. However, as we explore less favourable values of the quantities, the distributions shift to higher $|\Delta z|$ at any given value of the normalised counts. They also become less Gaussian, with flatter slopes and heavier tails at high $|\Delta z|$. The reason for this change in the shape of the $|\Delta z|$ distributions is an increase in the rate of catastrophic errors as we progress from left to right.

To identify which of these four quantities is more effective in separating the good from the bad photo-*z*, we cannot rely on Fig. 18 since the distribution of each of these quantities in the miniJPAS sample is different. Instead, we calculate the correlation of these quantities with $|\Delta z|$ for individual sources (Fig. 19). Because of the different ranges that each of these quantities span and the non-linearity of their relation with $|\Delta z|$, we compute correlations between ranks, instead of correlation of their values. That is, for each quantity (including $|\Delta z|$) we sort the galaxies in ascending order and compute the Spearman rank correlation coefficient (ρ). We find $\rho = 0.285, 0.466, 0.551$, and -0.602 for z_{best}, *r*-mag, z_{err}, and *odds*, respectively. In the case of the *odds* parameter, ρ is negative because the average $|\Delta z|$ decreases at higher *odds*. According to this, the *odds* parameter has the

strongest correlation with $|\Delta z|$, closely followed by z_{err}, then *r* while z_{best} has the weakest correlation.

This suggests that the best way to select a subsample of *N* galaxies with the most accurate photo-*z* is not to pick the *N* brightest galaxies in the sample (a cut in magnitude) or the *N* with smallest z_{err}, but the *N* with higher *odds*. The high dispersion in all panels of Fig. 19 implies that for individual galaxies or small samples that may not always be the case, but for large enough *N*, *odds* should have a clear advantage.

We confirm this hypothesis by computing σ_{NMAD} and η as a function of the fraction of the spectroscopic sample selected (f) with a threshold in any of these four quantities (Fig. 20). For f close to 1 (very few galaxies rejected), all four quantities yield almost the same σ_{NMAD} and η, since the samples selected are also nearly identical. However, as f decreases due to more restrictive thresholds, the tracks diverge. If we target a specific σ_{NMAD}, the size of the sample selected with a threshold in z_{err} or *odds* is significantly larger compared to a selection in *r*-band magnitude (up to ~50% larger for σ_{NMAD}~0.003). If, on the other hand, we target a specific sample size, the σ_{NMAD} obtained from the corresponding threshold in z_{err} or *odds* is also significantly smaller.

The curves of $\sigma_{\text{NMAD}}(f)$ for z_{err} and *odds* are nearly identical. This is no surprise, as the two parameters have a very strong anti-correlation (ρ=-0.856, Fig. 21), much stronger than any of them has with $|\Delta z|$.

It is remarkable that z_{err} and *odds* obtain the same σ_{NMAD} in the whole range of f and that it is significantly better than that of the *r*-band magnitude. However, z_{err} has much worse performance when it comes to avoiding outliers, in particular at $f<0.4$ where it is outperformed also by the *r*-band magnitude.

Our interpretation of these trends is as follows: for sources with a single significant peak in the *z*PDF, both z_{err} and *odds* depend on the width of the peak and produce similar ranks. However, in sources with multiple peaks in the *z*PDF z_{err} underestimates the actual uncertainty in z_{best} because it is blind to all but the highest peak. On the other hand, the *odds* is affected (decreased) by those secondary peaks. The consequence is that the galaxies with multiple peaks in the *z*PDF (which are more likely to have catastrophic redshift errors) get ranked higher by z_{err} compared to *odds*. This has almost no impact on σ_{NMAD} because it is insensitive to outliers, but it shows up in η, as many more outliers get ranks above the threshold in z_{err} compared to *odds*.

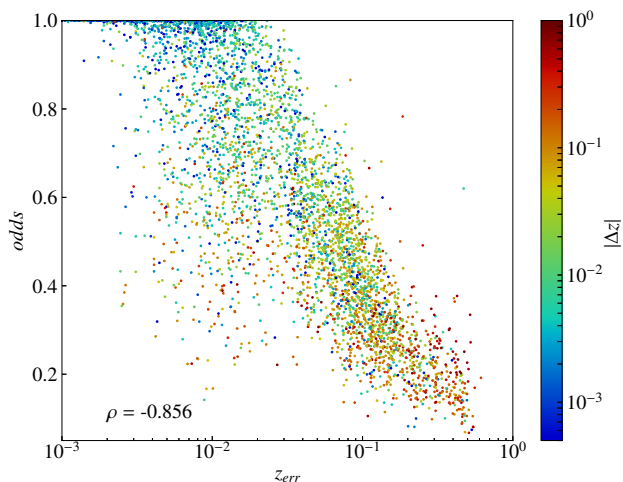## 6.4. Validation of z_{err} estimates

We have shown that z_{err} and *odds* are the quantities with the stronger correlation to Δz, and therefore the best choices for the selection of subsamples with the most accurate photo-*z*. In this section, we test if z_{err} corresponds to the actual 1-σ uncertainty in z_{best} for individual galaxies.

Figure 22 shows the distribution of $\Delta z/z_{err}$, which corresponds to the error in z_{best} in units of the predicted 1-σ uncertainty for each galaxy. Under ideal circumstances, the expected distribution is a Gaussian with a standard deviation of 1 (black line). However, the actual distribution is far from Gaussian, with a pointy core and extended tails. 55% of galaxies are within the [-1,1] interval and 77% in [-2,2] compared to expectations of 68% and 95%, respectively. The colour coding reveals that the core of the distribution is dominated by galaxies with high z_{err} values, while those with small z_{err} dominate in the tails. This suggests that sources with large (small) z_{err} overestimate (underestimate) the actual uncertainty in z_{best}.
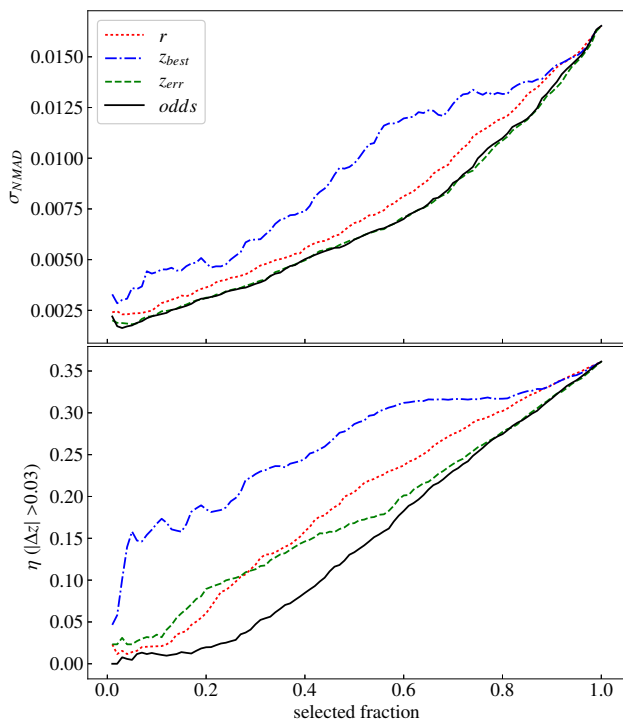
Fig. 20. Dependence of $\sigma_{\rm NMAD}$ and η on the fraction of the $r<23$ sample selected using a threshold in any of four different quantities: r-band magnitude, $z_{\rm best}$, z_{err}, and $odds$.


Fig. 21. Correlation between z_{err} and $odds$ for individual sources in the spectroscopic sample.

Further evidence is presented in Fig. 23 which shows the fraction of galaxies with $\Delta z < z_{err}$ as a function of z_{err} (grey histogram). If z_{err} estimates were accurate, this fraction should be constant around ~0.68 independently on z_{err}. Instead, we find a strong dependence with z_{err} for small z_{err} values with a fraction much lower than the expected 68%, while the relation becomes flat (but still below the expectation, with f~55–60%) for $z_{err} \gtrsim 0.003$.

One reason for the strong underestimation of the actual redshift uncertainty in sources with low z_{err} is the assumption implicit in the $\Delta\chi^2$ method that the probability distribution for the minimum of $\chi^2(z)$ is the χ^2 distribution for n degrees of freedom
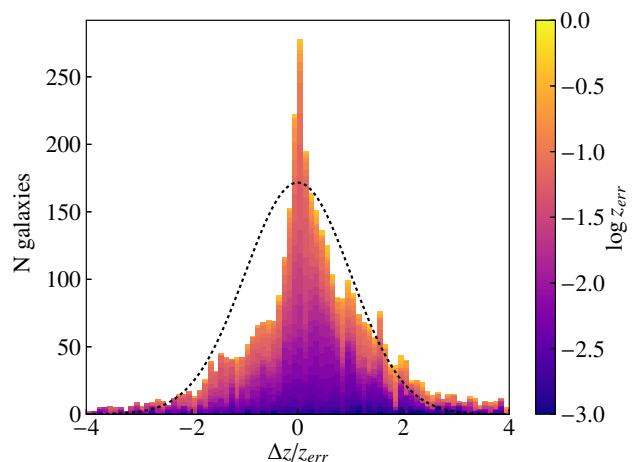
Fig. 22. Distribution of the ratio between the actual redshift error, Δz, and the uncertainty predicted with the $\Delta\chi^2$ method, z_{err}, for individual galaxies in the spectroscopic sample with colour coding for z_{err}.
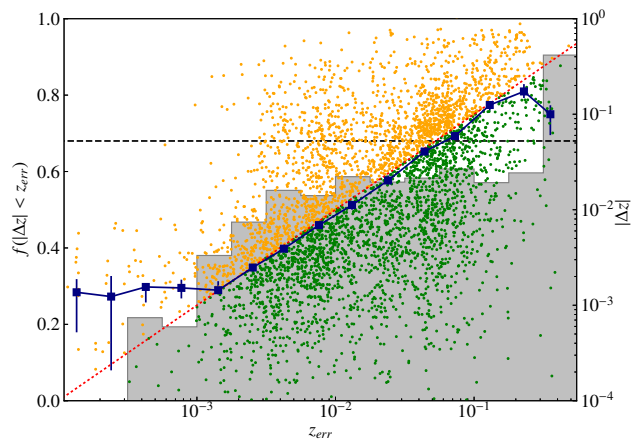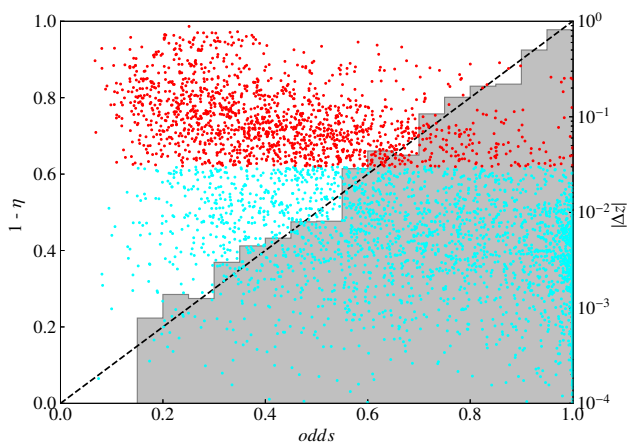

Fig. 23. Distribution of the fraction of galaxies with $|\Delta z| < z_{err}$ as a function of z_{err} (grey histogram). The horizontal line marks a fraction of 68% expected if z_{err} estimates are accurate. Small dots indicate the z_{err} and $|\Delta z|$ of individual galaxies (right hand scale). The dots are coloured orange and green for $|\Delta z| > z_{err}$ and $|\Delta z| < z_{err}$, respectively. The dotted red line marks the expected $\sigma_{\rm NMAD}$ as a function of z_{err}, while the connected dark blue squares with error bars indicate the $\sigma_{\rm NMAD}$ observed and the 16–84th percentiles of its confidence interval.

(Press et al. 1992). For bright sources with high S/N photometry, this is not the case since differences between the intrinsic SED of the galaxy and the closest template in the library are much larger than the photometric errors, implying large values for the reduced χ^2, $\chi^2_r = \chi^2/(n\text{-}1) \gg 1$ (see Hernán-Caballero 2012; Hernán-Caballero et al. 2015, for a discussion). By contrast, galaxies with low S/N photometry can easily get $\chi^2_r \lesssim 1$ with multiple redshift-template combinations due to degeneracy in the colour space. Since the model is not linear in the fitting parameters (namely the redshift and spectral type), the χ^2 distribution does not provide a realistic description of the actual redshift uncertainty (Oyaizu 2008).

Another factor contributing to the general overconfidence in z_{err} is the lack of sensitivity in the $\Delta\chi^2$ method to secondary peaks in the distribution of $\chi^2(z)$, and thus, to the probability of a catastrophic redshift error. This is evidenced by the close to

Fig. 24. Distribution of the fraction of sources with $|\Delta z| < 0.03$ as a function of *odds* (grey histogram). The diagonal line marks the 1:1 relation expected if *odds* estimates for individual galaxies are accurate. Small dots indicate the *odds* and $|\Delta z|$ of individual galaxies (right hand scale). The dots are coloured red for outliers ($|\Delta z| > 0.03$) or cyan otherwise.
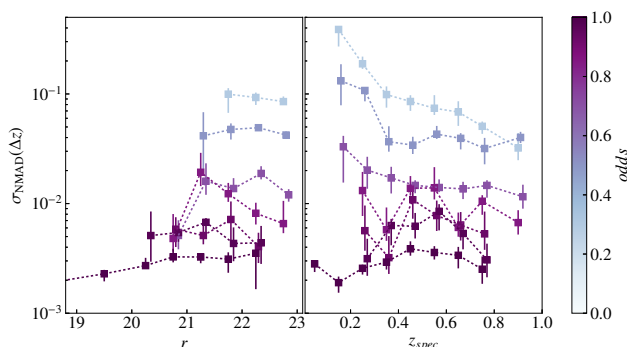
Fig. 25. Dependence of $\sigma_{\rm NMAD}$ on the *r*-band magnitude (left) and $z_{\rm spec}$ (right) for galaxies grouped in bins of *odds*. $\sigma_{\rm NMAD}$ is computed in steps of 0.5 (1 for $r<20$) for the *r*-band magnitude and 0.1 for redshift. Only bins containing more than 15 sources are shown.

1:1 relation between $\sigma_{\rm NMAD}$ and z_{err} in the range 0.001–0.1 (blue squares), which shows that for $z_{err}>0.001$, it is in fact a realistic prediction of the error in $z_{\rm best}$ if catastrophic errors are excluded.

6.5. Validation of *odds* estimates

Our definition of the *odds* parameter (see Sect. 4.4) implies that for an individual galaxy, the probability of an error $|\Delta z|>0.03$ in $z_{\rm best}$ is $P = 1 - odds$. Therefore, for a sufficiently large subsample, the outlier rate should be $\eta \approx 1 - \langle odds \rangle$.

Since the *z*PDF used to compute the *odds* is derived from $\chi^2(z)$ and the redshift prior, it is affected by the same $\chi^2_r \gg 1$ issue that we discussed for z_{err}. However, we compensated for this with the contrast correction applied to the *z*PDF in Sect. 4.3. Also, unlike z_{err}, the *odds* is sensitive to the presence of secondary peaks in the *z*PDF, meaning it should accurately estimate the probability of being an outlier for individual galaxies. We test this in Fig. 24 which shows that the fraction of galaxies with $|\Delta z|<0.03$ has the expected dependence with the *odds* in the whole range (note that $f(|\Delta z|<0.03) = 1 - \eta$).

To check whether the magnitude or redshift of the galaxies has any impact on photo-z accuracy that is not already accounted

for by the *odds*, we show in Fig. 25 the magnitude and redshift dependence of $\sigma_{\rm NMAD}$ at constant *odds*. There is no clear residual dependence of $\sigma_{\rm NMAD}$ with the *r*-magnitude. However, there seems to be an increase in $\sigma_{\rm NMAD}$ at low *z*, in particular for sources with very low *odds*. This might be a consequence of the redshift prior favouring intermediate $z_{\rm best}$ values in faint sources with low S/N (the prior probability peaks at $z{\sim}0.6$ for $r=22$ and $z{\sim}0.75$ for $r=23$, see Fig. 7). Since the number of galaxies with low *z* and low *odds* is small, we do not expect this to have a significant impact on our results.

6.6. Dependence on the spectral type

Photo-z accuracy is also expected to depend on the spectral type of the galaxies, which determines the contrast of the spectral features that anchor the photo-z. The most important such features at the redshifts typical of miniJPAS galaxies are the 4000 Å break of the stellar continuum and the main optical emission lines (Hα, Hβ, [O II] 3727 Å and [O III] 4959+5007 Å).

The combination of deep broad-band and shallower narrow-band photometry produces some interesting trends for miniJPAS galaxies: at relatively bright magnitudes the narrow-band filters easily detect emission lines, if they are present, which increases the chances of a highly accurate photo-z in star-forming galaxies compared to quiescent ones. However, as we move to fainter magnitudes, the emission lines become increasingly hard to detect, removing the advantage for star-forming galaxies. At magnitudes fainter than the detection limit in the narrow bands, it is quiescent galaxies that often have an edge due to their stronger 4000 Å break which is easily detected in the broad-band photometry.

To quantify the impact of the spectral type on $\sigma_{\rm NMAD}$, we have classified all the galaxies in the spectroscopic sample into two broad categories "red" and "blue", loosely corresponding to quiescent and star-forming, respectively. We repeat the classification three times, according to the value of three different parameters from the best-fitting CIGALE model: (1) $D_n(4000)$, which measures the strength of the 4000 Å break using the definition of Balogh et al. (1999) and is a proxy for the light-weighted age of the stellar population (e.g. Kauffmann et al. 2003a,b; Kriek et al. 2006; Hernán-Caballero et al. 2013); (2) the specific instantaneous star formation rate (sSFR) derived directly from the model star formation history; (3) the equivalent width of the Hα line (EW(Hα)), an observational proxy for the sSFR.

Since the boundary between the quiescent and star-forming classes is somewhat arbitrary (there are many galaxies with intermediate properties) and is also redshift- and luminosity-dependent, we simplify the classification by splitting the sample into two same-sized subsamples. The first (second) subsample contains the 50% of galaxies with the highest (lowest) value of $D_n(4000)$, sSFR, or EW(Hα). Such criteria do not provide high purity in the resulting samples of quiescent and star-forming galaxies but allow to compare more easily the results between the different selection criteria, and is sufficient to check whether the *odds* parameter accounts for the dependence on the spectral type.

Figure 26 shows the $\sigma_{\rm NMAD}$ for all sources brighter than a given *r*-band magnitude cut in the "red" and "blue" samples. The trends are similar irrespective of the quantity used to split the sample but there are some interesting differences: for a cut at very faint magnitudes ($r\lesssim 23$), the red sample gets lower $\sigma_{\rm NMAD}$ when the selection is done with $D_n(4000)$ or sSFR but not with EW(Hα). This indicates that a substantial number of
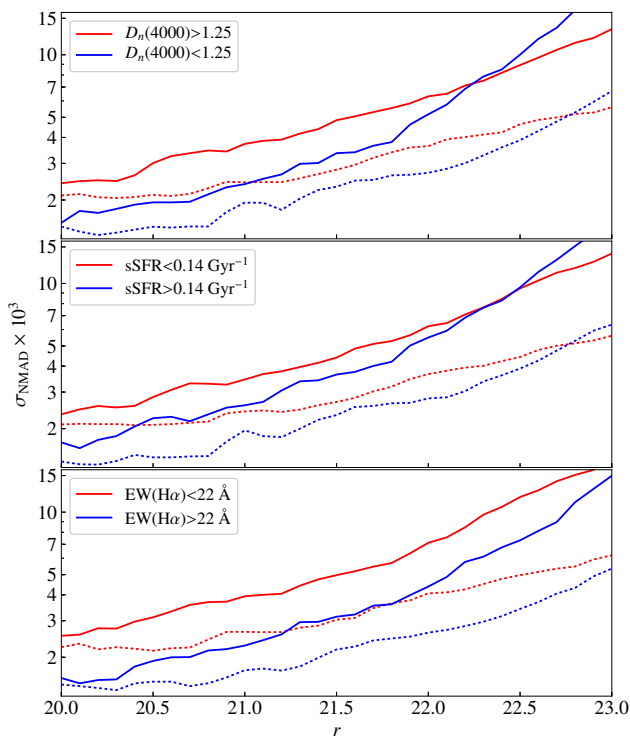
Fig. 26. Variation of σ_{NMAD} as a function of the cut applied in r-band magnitude separately for "red" and "blue" galaxies. Each panels shows results for a different way to classify the galaxies, using the strength of the 4000 Å break (top), the specific instantaneous SFR (middle), and the equivalent width of Hα (bottom). Solid lines correspond to σ_{NMAD} values at 100% completeness (no cut in $odds$), while dotted lines indicate σ_{NMAD} values for a cut in $odds$ corresponding to 50% completeness.

galaxies switches between the red and blue classes depending on the parameter used. Classifying with EW(Hα) puts some high D_n(4000) galaxies (that for some reason, maybe active nuclei, also have Hα emission) in the blue sample, improving its σ_{NMAD}.

A consequence of this is that the photo-z accuracy at a given magnitude depends not only on the spectral type but on how the spectral type is defined. In particular, more restrictive classification criteria are likely to improve the photo-z accuracy for both quiescent and star-forming galaxies, since it is intermediate cases (where neither the 4000 Å break nor emission lines are strong) that constitute the most difficult targets for photo-z calculation.

The factors responsible for the different photo-z accuracy in quiescent and star-forming galaxies are also reflected in the value of the $odds$ parameter. Figure 27 shows that if the comparison is made between galaxies within a narrow range of $odds$, the difference in σ_{NMAD} between red and blue galaxies disappears. The similarity is even stronger for η, indicating that the $odds$ parameter accurately predicts the probability of a catastrophic error for both quiescent and star-forming galaxies.

6.7. Representativeness of the spectroscopic sample

The photo-z performance statistics presented so far refer only to the subsample of miniJPAS galaxies with spectroscopic redshifts (s-sample). We can expect these statistics to also predict the performance in the sources with no spectroscopic redshifts
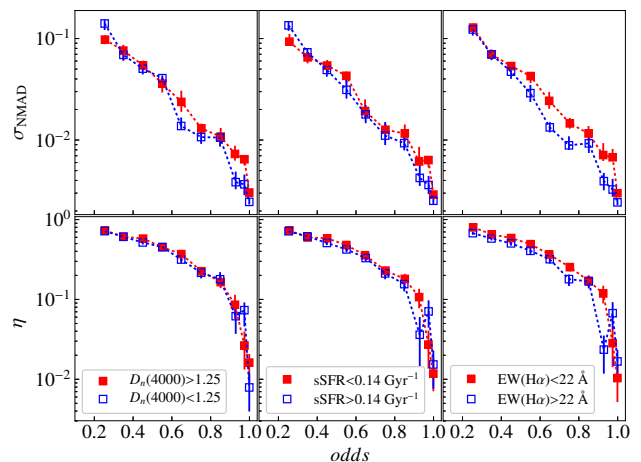
Fig. 27. Dependence of σ_{NMAD} and η with $odds$ for "quiescent" (red solid symbols) and "star-forming" (blue open symbols) galaxies in the spectroscopic sample according to three different classification criteria (left, center, and right panels, see text for details). The error bars represent 1-σ confidence intervals calculated with bootstrap resampling.
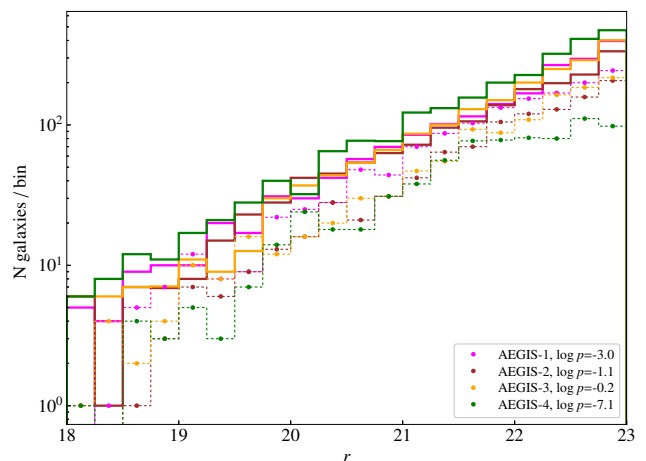
Fig. 28. Distribution of the observed r-band magnitude of miniJPAS galaxies for the photo-z-only sample (solid lines) and the spectroscopic sample (connected dots) for individual pointings. $\log p$-values in the legend indicate the probability of the spectroscopic and photo-z-only samples being drawn from the same parent population.

(p-sample) only if the s- and p-sample are drawn from the same parent population.

We already showed in Fig. 4 that the distribution of r-band magnitude in the s-sample reproduces that of the whole miniJPAS when every source is weighted with its probability of being a galaxy, P_G. Figure 28 presents a more detailed comparison of the magnitude distribution in the s-sample and p-sample. Since the spectroscopic coverage and the depth of the miniJPAS images varies from one pointing to another, we show the distributions for each pointing separately. We use the two-sample Kolmogorov-Smirnov test to calculate the probability p of the s-sample and p-sample being drawn from the same parent population. The difference between samples is significant ($p<0.01$) only for pointing AEGIS-4. Unlike the other pointings, the spectroscopic counts in AEGIS-4 flatten at $r>21.5$. Interestingly, this pointing has the smallest area covered by DEEP and the lowest number of spectroscopic galaxies and, as a consequence,

Table 1. Average colour indices by magnitude

colour index	18<*r*<20		20<*r*<22		22<*r*<23	
	phot	spec	phot	spec	phot	spec
$\langle u-r \rangle$	2.051	2.028	1.351	1.257	0.208	0.201
$\langle g-r \rangle$	1.035	1.123	1.086	1.096	0.875	0.871
$\langle g-i \rangle$	1.479	1.578	1.552	1.590	1.307	1.345
$\langle r-i \rangle$	0.444	0.455	0.469	0.498	0.480	0.520
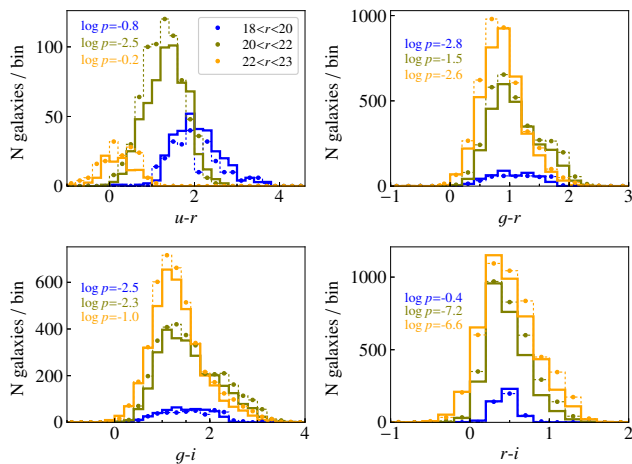
Fig. 29. Distribution of the observed broad-band colours in three bins of magnitude. Each plot includes only sources with >3σ detections in the two bands defining the colour index and with valid photo-*z* estimates. Solid lines show the distributions measured for galaxies in the photo-*z*-only sample. Connected dots represent the distribution for galaxies in the spectroscopic sample (scaled by a factor 2 to facilitate the comparison).

also the highest counts of photo-*z*-only galaxies in almost every magnitude bin. The presence of a large galaxy cluster centred at RA=213.6254, DEC=51.9379 (see Fig. 28 in **B21**) may also boost the galaxy counts in AEGIS-4.

In Fig. 29, we compare the distributions of four broad-band colours for galaxies in the *p*-sample and *s*-sample. For each colour index, only sources with >3σ detection in both bands are considered. We show the distributions separately for three magnitude ranges. The magnitude-dependence of the colour distribution is small except for the *u-r* colour, where the S/N>3 requirement for the *u* band implies that most red objects are not selected at faint magnitudes, shifting the distribution towards bluer *u-r*. Discrepancies between distributions for the *s*-sample and *p*-sample are highly significant, particularly for the *r-i* colour in *r*>20 sources (*p*<0.0001). However, the range of colour indices covered are the same and, in all cases, the mean colour index of the distribution differs by less than 0.1 magnitudes (Table 1).

The distribution of $z_{\rm best}$ (left panel in Fig. 30) is slightly biased towards higher values for *r*>20 sources in the *s*-sample compared to the *p*-sample. This is consistent with their redder *g-i* and *r-i* colours. For the *odds* parameter (right panel), the difference is significant only among the faintest galaxies (*r*>22) and indicates that *r*>22 galaxies have higher *odds*, on average, in the *s*-sample compared to the *p*-sample. This may be a consequence of the requirement of a high confidence in the spectroscopic redshift for selection into the *s*-sample. At faint magnitudes, such confidence requires high contrast spectral features (a strong 4000 Å break or emission lines) that also help increase the confidence in the photo-*z* estimate.
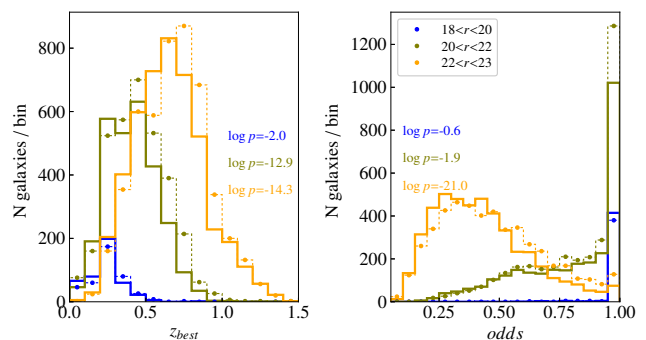
Fig. 30. Distribution of $z_{\rm best}$ and *odds* in bins of magnitude for the photo-*z*-only and spectroscopic samples. Symbols as in Fig. 29.

As a result of this analysis, we conclude that the *s*-sample is slightly biased towards redder and more distant galaxies but also with higher *odds* compared to same-magnitude galaxies in the *p*-sample. However, such small differences do not suggest the existence of a population of galaxies in the *p*-sample that is not represented in the *s*-sample. Accordingly, we consider the templates selected for the *s*-sample to also be suitable for the *p*-sample and we expect a similar performance.

The small but highly significant differences in the *odds* distributions are important since the strong correlation between *odds* and photo-*z* accuracy implies that for magnitude-limited subsamples the $\sigma_{\rm NMAD}$ and η measured in the *s*-sample probably overestimate the actual accuracy in the *p*-sample. However, we have shown that *odds* is the best predictor of photo-*z* accuracy and that, at constant *odds*, the residual dependence of photo-*z* accuracy with *r*, $z_{\rm spec}$, or the spectral type is small.

This implies that the distribution of |Δz| at a given *odds* obtained for the *s*-sample should also represent that of the *p*-sample. In the next section we show how to use this to compensate for the different *odds* distributions in the *s*- and *p*-sample to obtain realistic photo-*z* performance statistics for the *p*-sample.

6.8. Extrapolation to the entire miniJPAS sample

The spectroscopic sample used for all the analysis up to this point excludes sources with flags in the photometry. In order to check the impact of photometric flags in the photo-*z* accuracy, we compare in Fig. 31 the values of $\sigma_{\rm NMAD}$ and η as a function of *odds* for flagged and non-flagged galaxies in the spectroscopic sample. The differences in $\sigma_{\rm NMAD}$ are minimal and largely consistent within the statistical errors except at very low *odds* (*odds*<0.4). This suggest that most flagged sources are barely affected in their photo-*z* accuracy by the photometric issue signalled by the flags. The trends for η are also very similar except at *odds*>0.9, where the outlier rate stays at η~0.1 for flagged sources while it falls down to η~0.01 for non-flagged ones. This clear excess of outliers at very high *odds* is probably a consequence of strong spurious peaks in the *z*PDF caused by artefacts in the photometry of some of the flagged sources. Since flagged sources represent ~30% of the miniJPAS sample, we consider that such a small increase in the outlier rate relative to non-flagged ones does not justify purging flagged sources unless very high reliability (very low η) is required.

The strong dependence of the distribution of |Δz| with *odds* (Fig. 18) and the lack of a significant residual dependence with other quantities at constant *odds* allow us to estimate the number
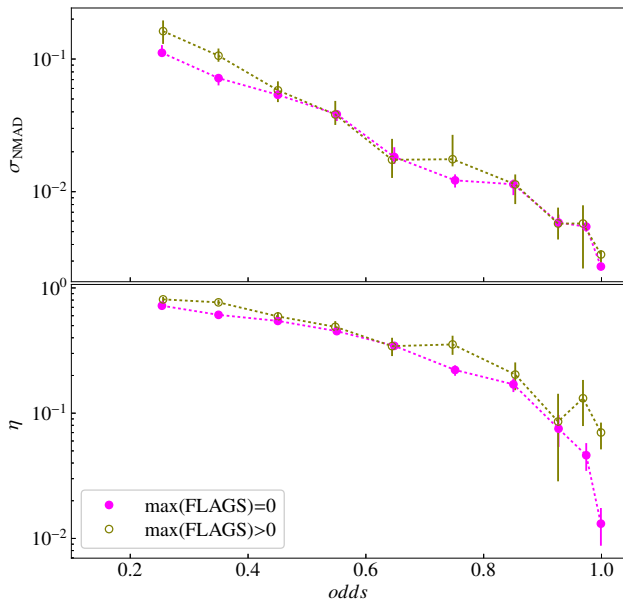
Fig. 31. Dependence of σ_{NMAD} (top) and η (bottom) with *odds* for sources in the spectroscopic sample with no photometry flags in any bands (solid symbols) and sources with flags in one or more bands (open symbols).

of galaxies with photo-*z* errors below a given threshold in any arbitrary sample of miniJPAS sources:

$$N(|\Delta z| < \Delta z') = \sum_i P_{G,i} \, f_S(|\Delta z| < \Delta z' \mid odds_i) \tag{13}$$

where $P_{G,i}$ is the probability of being a galaxy for source i (see Sect. 2.4) and $f_S(|\Delta z| < \Delta z' \mid odds_i)$ is the frequency of $|\Delta z| < \Delta z'$ among galaxies with $odds \approx odds_i$ in the spectroscopic sample. Table 2 lists the values of $f_S(|\Delta z| < \Delta z' \mid odds)$ calculated for intervals of *odds* with several values of the threshold $\Delta z'$.

We use Eq. 13 to compute the number density n of galaxies in miniJPAS with $r < 23$ and $|\Delta z| < \Delta z'$ for several cuts in *odds* (Fig. 32). For this we assume that the effective area of miniJPAS (after taking the masked areas into account) is 0.895 deg^2 (see B21). We repeat the calculation twice: first using the frequencies $f_S(|\Delta z| < \Delta z' \mid odds)$ calculated on non-flagged sources for flagged and non-flagged ones indistinctly; second using their own $f_S(|\Delta z| < \Delta z' \mid odds)$ for both flagged and non-flagged sources. The difference in number counts between the two methods is <3% for any $\Delta z'$ and cut in *odds*.

These distributions show that there are ~17,500 galaxies per deg^2 in miniJPAS at $r < 23$, of which ~4,200 have $|\Delta z| < 0.003$. However, selecting all of them requires to put no constraint in *odds*, which results in large average errors ($\sigma_{\mathrm{NMAD}} = 0.013$) and high rate of outliers ($\eta = 0.39$). The targeted photo-*z* accuracy for J-PAS ($\sigma_{\mathrm{NMAD}} = 0.003$; Benítez et al. 2014) is achieved after imposing $odds > 0.82$, that implies selecting ~5,200 galaxies per deg^2 (of which ~2,600 have $|\Delta z| < 0.003$ and only ~5% are outliers).

7. Summary

This paper describes the procedures that we followed in order to generate the photo-*z* catalogue of miniJPAS, a ~1 deg^2 imaging survey in 60 optical bands encompassing the AEGIS field. We

Table 2. Fraction of sources with $|\Delta z| < \Delta z'$ per *odds* interval in the spectroscopic sample

odds	N_{spec}	$\Delta z'=0.003$	$\Delta z'=0.01$	$\Delta z'=0.03$	$\Delta z'=0.1$
0.025–0.075	3	0.333	0.333	0.333	0.667
0.075–0.125	29	0.103	0.172	0.207	0.379
0.125–0.175	102	0.059	0.157	0.216	0.441
0.175–0.225	150	0.080	0.160	0.270	0.533
0.225–0.275	210	0.055	0.133	0.227	0.510
0.275–0.325	244	0.074	0.213	0.369	0.631
0.325–0.375	249	0.121	0.265	0.402	0.735
0.375–0.425	249	0.113	0.221	0.378	0.763
0.425–0.475	247	0.115	0.296	0.489	0.838
0.475–0.525	250	0.109	0.284	0.475	0.852
0.525–0.575	239	0.159	0.326	0.524	0.879
0.575–0.625	235	0.151	0.396	0.641	0.906
0.625–0.675	205	0.210	0.454	0.650	0.941
0.675–0.725	198	0.180	0.485	0.703	0.939
0.725–0.775	145	0.239	0.572	0.801	0.966
0.775–0.825	189	0.236	0.550	0.805	0.963
0.825–0.875	159	0.259	0.566	0.827	0.962
0.875–0.925	155	0.378	0.710	0.882	0.981
0.925–0.975	223	0.355	0.767	0.956	0.996
0.975–1.000	827	0.596	0.921	0.981	0.993
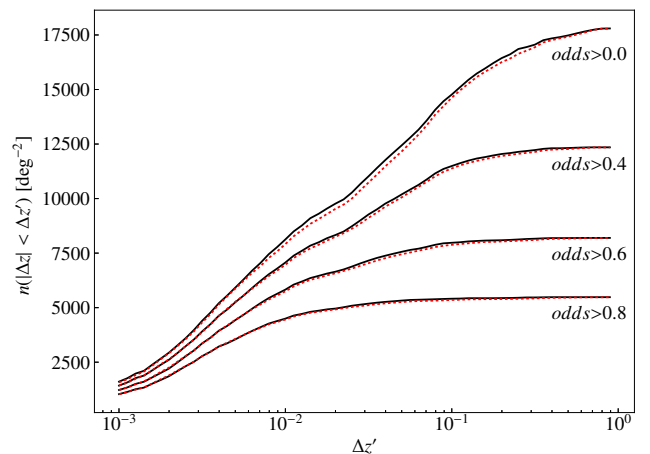
Fig. 32. Predicted density of $r < 23$ miniJPAS galaxies with redshift errors $|\Delta z| < \Delta z'$ as a function of the threshold $\Delta z'$ for four different cuts in the *odds* parameter. The solid lines are generated by applying the same value of $f_S(|\Delta z| < \Delta z' \mid odds_i)$ calculated in non-flagged sources to both flagged and non-flagged ones, while the dotted lines uses separate values for flagged and non-flagged sources.

also provide a detailed analysis of the photo-*z* performance enabled by the exhaustive spectroscopic coverage of AEGIS by the SDSS and DEEP surveys.

We rely on forced (dual mode) photometry obtained for a *r*-band selected catalogue with matched apertures corresponding to 1 Kron radius in the *r* band (restricted AUTO aperture), with corrections to compensate for the difference in the PSF of each band with respect to *r* (PSFCOR photometry).

We use CIGALE to generate stellar population synthesis models matching the photo-spectra of all $r < 22$ galaxies with spectroscopic redshifts. Synthetic photometry obtained from these models is used to identify systematic offsets in the observed photometry with respect to the models. We show that an iterative correction of these offsets converges to the same solution within ~0.01 magnitudes irrespective of the initial offsets.

The photo-*z* are computed with a customised version of LePHARE. The spectral templates used are the best-fitting CIGALE mod-

els of 50 miniJPAS galaxies, selected from a larger set of 455 candidates as the ones that produce the most accurate photo-z in a test sample.

We show that the redshift probability distribution functions (zPDF) generated by LePhare are slightly overconfident for $r<19$ galaxies but severely under-confident at $r>20$. A simple contrast correction of the zPDF compensates for this magnitude dependence.

Comparison between the mode of the zPDF (z_{best}) and the spectroscopic redshift (z_{spec}) shows that the distribution of absolute redshift errors ($|\Delta z|$) is bimodal. The main peak at $|\Delta z|\sim0.004$ corresponds to the typical inaccuracy in photo-z estimates while a second peak at $|\Delta z|\sim0.04$ represents catastrophic errors.

The distribution of z_{best} for the galaxies in miniJPAS closely follows the distribution of z_{spec} in the spectroscopic subsample. This indicates that (1) the spectroscopic sample is representative of the redshift distribution of the whole sample and (2) we successfully detect variation in the density of galaxies along the redshift dimension, at least up to $z\sim0.8$.

We find z_{best} estimates are biased towards $z_{best}>z_{spec}$ by ~0.10–0.14%. This bias is consistent among the four miniJPAS pointings and shows no clear dependence with either the magnitude or the redshift of the sources. In spite of our efforts to identify the origin of this bias, it remains uncertain and demands further analysis.

The *odds* parameter has the strongest correlation to $|\Delta z|$ of any photo-z related quantities. In particular, its correlation is significantly stronger than obtained with the predicted 1-σ redshift error (z_{err}) since the latter is insensitive to the probability of a catastrophic redshift error. This implies that applying a cut in *odds* is the most efficient way to select a fixed-size subsample with the best possible photo-z (or, conversely, the largest sample within some photo-z quality constraints). We also show that there is no clear residual dependence of the photo-z accuracy with the r-band magnitude at constant *odds*, while there seems to be a redshift dependence for sources with very low *odds*, consistent with the expected effect of the redshift prior in low S/N photometry.

Comparison of z_{err} and $|\Delta z|$ shows that the former increasingly underestimates the actual errors in z_{best} for lower z_{err} values. On the other hand, the *odds* parameter accurately represents the probability of a redshift outlier ($|\Delta z|>0.03$).

The photo-z accuracy is dependent on the spectral type. Emission lines allow star-forming galaxies to obtain lower σ_{NMAD} compared to quiescent ones at bright magnitudes but their advantage vanishes at faint magnitudes as the emission lines become increasingly hard to detect and the photo-z solution becomes dominated by the 4000 Å break. The dependence on the spectral type disappears if σ_{NMAD} or η are calculated for sources within narrow intervals of *odds*.

We confirm that the distribution of magnitudes and broad-band colours in the spectroscopic sample is roughly consistent with the photo-z-only sample, albeit galaxies in the latter are slightly bluer ($\lesssim0.1$ magnitudes) and have slightly lower z_{best} on average. The distribution of *odds* for $r>22$ galaxies is also biased towards higher values in the spectroscopic sample. We take this into account to generate realistic estimates of the expected photo-z accuracy in the photo-z-only sample.

We conclude that at the depth of miniJPAS, there are $\sim17,500$ galaxies per deg^2 with valid photo-z estimates, of which $\sim4,200$ have $|\Delta z|<0.003$. The typical error for $r<23$ galaxies is $\sigma_{NMAD}=0.013$ with an outlier rate $\eta=0.39$. The target photo-z accuracy $\sigma_{NMAD}=0.003$ is achieved after imposing *odds*>0.82. Under such constraint, the density of galaxies selected is reduced by 70% to $n\sim5,200$ deg^{-2} (of which $\sim2,600$ have $|\Delta z|<0.003$) and the outlier rate decreases to $\eta=0.05$.

References

Alarcon, A., Gaztanaga, E., Eriksen, M., et al. 2021, MNRAS, 501, 6103

Angulo, R. E., Baugh, C. M., Frenk, C. S., et al. 2008, MNRAS, 383, 755

Avni Y., 1976, ApJ, 210, 642

Arnouts, S., & Ilbert, O. 2011, LePHARE: Photometric Analysis for Redshift Estimate, ascl:1108.009

Balogh, M. L., Morris, S. L., Yee, H. K. C., et al. 1999, ApJ, 527, 54

Baqui, P. O., Marra, V., Casarini, L. et al. 2020, A&A submitted, arXiv:2007.07622

Baum, W. A. 1962, Problems of Extra-Galactic Research, 15, 390

Benítez, N., Moles, M., Aguerri, J. A. L., et al. 2009, ApJ, 692, L5

Benítez, N., Dupke, R., Moles, M., et al. 2014, arXiv e-prints, arXiv:1403.5237

Benítez, N. 2000, ApJ, 536, 571

Bertin, E. & Arnouts, S. 1996, A&AS, 117, 393

Bertin, E., Mellier, Y., Radovich, M., et al. 2002, Astronomical Data Analysis Software and Systems XI, 281, 228

Bertin, E. 2006, Astronomical Data Analysis Software and Systems XV, 351, 112

Blake, C. & Bridle, S. 2005, MNRAS, 363, 1329

Bolzonella M., Miralles J. M., Pelló R., 2000, A&A, 363, 476

Bonoli, S., Marín-Franch, A., Varela, J., et al. 2020, A&A, in press. arXiv:2007.01910

Boquien, M., Burgarella, D., Roehlly, Y., et al. 2019, A&A, 622, A103

Brammer, G. B., van Dokkum, P. G., & Coppi, P. 2008, ApJ, 686, 1503

Bruzual, G., & Charlot, S. 2003, MNRAS, 344, 1000

Calzetti, D., Armus, L., Bohlin, R. C., et al. 2000, ApJ, 533, 682

Chabrier, G. 2003, PASP, 115, 763

Chaves-Montero, J., Angulo, R. E., & Hernández-Monteagudo, C. 2018, MNRAS, 477, 3892

Coe, D., Benítez, N., Sánchez, S. F., et al. 2006, AJ, 132, 926

Coil, A. L., Newman, J. A., Kaiser, N., et al. 2004, ApJ, 617, 765

Cooper, M. C., Aird, J. A., Coil, A. L., et al. 2011, ApJS, 193, 14

Couch, W. J., Ellis, R. S., Godwin, J., et al. 1983, MNRAS, 205, 1287

Dahlen T. et al., 2013, ApJ, 775, 93

Davis, M., Faber, S. M., Newman, J., et al. 2003, SPIE, 4834, 161

Eriksen, M., Alarcon, A., Gaztanaga, E., et al. 2019, MNRAS, 484, 4200

Ferland, G. J., Korista, K. T., Verner, D. A., et al. 1998, PASP, 110, 761

Ferland, G. J., Porter, R. L., van Hoof, P. A. M., et al. 2013, RMxAA, 49, 137

Fernández-Soto, A., Lanzetta, K. M., & Yahil, A. 1999, ApJ, 513, 34

Fernández-Soto A., Lanzetta K. M., Chen H.-W., Levine B., Yahata N., 2002, MNRAS, 330, 889

González Delgado, R. M., Díaz-García, L. A., de Amorim, A., et al. 2021, A&A, in press. arXiv:2102.13121

Green, G. M., Schlafly, E. F., Finkbeiner, D., et al. 2018, MNRAS, 478, 651

Hernán-Caballero A., et al., 2013, MNRAS, 434, 2136

Hernán-Caballero, A., Alonso-Herrero, A., Hatziminaoglou, E., et al. 2015, ApJ, 803, 109

Hernán-Caballero, A. 2012, MNRAS, 427, 816

Hildebrandt, H., Wolf, C., & Benítez, N. 2008, A&A, 480, 703

Ilbert, O., Arnouts, S., McCracken, H. J., et al. 2006, A&A, 457, 841

Inoue, A. K. 2011, MNRAS, 415, 2920

Kauffmann G., et al. 2003a, MNRAS, 341, 33

Kauffmann G., et al. 2003b, MNRAS, 341, 54

Kriek M., et al., 2006, ApJ, 645, 44

Kron, R. G., 1980, ApJS, 43, 305

Lanzetta, K. M., Yahil, A., & Fernández-Soto, A. 1996, Nature, 381, 759

López-Sanjuan, C., Vázquez Ramió, H., Varela, J., et al. 2019a, A&A, 622, A177

López-Sanjuan, C., Varela, J., Cristóbal-Hornillos, D., et al. 2019b, A&A, 631, A119

Le Fèvre, O., Vettolani, G., Garilli, B., et al. 2005, A&A, 439, 845

Mobasher, B., Rowan-Robinson, M., Georgakakis, A., et al. 1996, MNRAS, 282, L7

Moles, M., Benítez, N., Aguerri, J. A. L., et al. 2008, AJ, 136, 1325

Molino, A., Benítez, N., Moles, M., et al. 2014, MNRAS, 441, 2891

Molino, A., Costa-Duarte, M. V., Mendes de Oliveira, C., et al. 2019, A&A, 622, A178

Molino, A., Benítez, N., Ascaso, B., et al. 2017, MNRAS, 470, 95

Mundy, C. J., Conselice, C. J., Duncan, K. J., et al. 2017, MNRAS, 470, 3507

Newman, J. A., Cooper, M. C., Davis, M., et al. 2013, ApJS, 208, 5

Noll, S., Burgarella, D., Giovannoli, E., et al. 2009, A&A, 507, 1793

Oyaizu H., Lima M., Cunha C. E., Lin H., Frieman J., 2008, ApJ, 689, 709

Pérez-González, P. G., Cava, A., Barro, G., et al. 2013, ApJ, 762, 46

Polsterer, K. L., D'Isanto, A., & Gieseke, F. 2016, arXiv:1608.08016

Press W. H., Teukolsky S. A., Vetterling W. T., Flannery B. P., 1992, Numerical Recipes in C: The Art of Scientific Computing, 2nd edn. Cambridge Univ. Press, Cambridge

Salvato, M., Ilbert, O., & Hoyle, B. 2019, Nature Astronomy, 3, 212

Schlafly, E. F., Meisner, A. M., Stutz, A. M., et al. 2016, ApJ, 821, 78

Schmidt, S. J., Malz, A. I., Soo, J. Y. H., et al. 2020, MNRAS, 499, 1587

Schmidt S. J., Thorman P., 2013, MNRAS, 431, 2766

Taniguchi, Y., Scoville, N., Murayama, T., et al. 2007, ApJS, 172, 9

Taniguchi, Y., Kajisawa, M., Kobayashi, M. A. R., et al. 2015, PASJ, 67, 104

Whitten, D. D., Placco, V. M., Beers, T. C., et al. 2019, A&A, 622, A182

Wittman D., Bhaskar R., Tobin R., 2016, MNRAS, 457, 4005

Wolf, C., Meisenheimer, K., Rix, H. W., et al. 2003, A&A, 401, 73

York, D. G., Adelman, J., Anderson, John E., J., et al. 2000, AJ, 120, 1579

Table 3. zeropoint recalibration offsets [mag]

band	AEGIS-1	AEGIS-2	AEGIS-3	AEGIS-4
uJAVA	0.200 ± 0.043	0.099 ± 0.044	0.056 ± 0.064	0.039 ± 0.051
J0378	0.014 ± 0.042	0.015 ± 0.040	0.161 ± 0.089	-0.139 ± 0.075
J0390	0.331 ± 0.023	0.114 ± 0.033	0.124 ± 0.045	0.032 ± 0.043
J0400	0.225 ± 0.028	0.090 ± 0.035	0.163 ± 0.050	0.250 ± 0.041
J0410	0.196 ± 0.035	0.119 ± 0.042	0.235 ± 0.050	-0.006 ± 0.057
J0420	0.230 ± 0.037	0.040 ± 0.046	0.035 ± 0.063	0.008 ± 0.058
J0430	0.105 ± 0.034	0.099 ± 0.032	0.119 ± 0.060	0.058 ± 0.030
J0440	0.439 ± 0.029	0.156 ± 0.039	0.141 ± 0.045	0.084 ± 0.038
J0450	0.082 ± 0.039	-0.017 ± 0.051	0.050 ± 0.074	0.065 ± 0.051
J0460	0.192 ± 0.015	0.160 ± 0.021	0.103 ± 0.044	0.123 ± 0.030
J0470	0.191 ± 0.021	0.109 ± 0.027	0.166 ± 0.035	0.336 ± 0.034
J0480	0.232 ± 0.022	0.131 ± 0.032	0.206 ± 0.032	0.119 ± 0.032
J0490	0.219 ± 0.026	0.072 ± 0.037	0.070 ± 0.040	0.105 ± 0.057
J0500	0.080 ± 0.015	0.098 ± 0.026	0.101 ± 0.031	0.070 ± 0.024
J0510	0.416 ± 0.023	0.156 ± 0.026	0.095 ± 0.023	0.047 ± 0.025
J0520	0.042 ± 0.031	-0.042 ± 0.028	0.082 ± 0.037	0.012 ± 0.035
J0530	0.234 ± 0.016	0.065 ± 0.021	0.038 ± 0.016	0.069 ± 0.038
J0540	0.174 ± 0.019	0.038 ± 0.021	0.130 ± 0.023	0.175 ± 0.025
J0550	0.145 ± 0.019	0.085 ± 0.027	0.127 ± 0.022	0.078 ± 0.031
J0560	0.209 ± 0.018	0.024 ± 0.025	0.047 ± 0.029	0.037 ± 0.041
J0570	0.086 ± 0.016	0.051 ± 0.023	0.067 ± 0.022	0.044 ± 0.028
J0580	0.403 ± 0.017	0.070 ± 0.021	0.088 ± 0.016	0.046 ± 0.021
J0590	0.121 ± 0.026	-0.024 ± 0.016	0.061 ± 0.028	-0.017 ± 0.027
J0600	0.126 ± 0.017	0.065 ± 0.019	0.131 ± 0.019	0.043 ± 0.026
J0610	0.112 ± 0.017	0.063 ± 0.019	0.109 ± 0.016	0.182 ± 0.019
J0620	0.178 ± 0.021	0.084 ± 0.021	0.110 ± 0.019	0.052 ± 0.031
J0630	0.185 ± 0.015	0.015 ± 0.021	0.026 ± 0.020	0.045 ± 0.031
J0640	0.101 ± 0.016	0.054 ± 0.019	0.103 ± 0.011	0.016 ± 0.020
J0650	0.335 ± 0.017	0.087 ± 0.020	0.042 ± 0.010	0.045 ± 0.019
J0660	0.133 ± 0.010	0.102 ± 0.016	0.129 ± 0.007	0.089 ± 0.031
J0670	0.253 ± 0.015	0.056 ± 0.014	0.089 ± 0.007	0.102 ± 0.024
J0680	0.099 ± 0.016	0.074 ± 0.016	0.082 ± 0.008	0.109 ± 0.033
J0690	0.151 ± 0.018	0.076 ± 0.021	0.076 ± 0.019	0.031 ± 0.032
J0700	0.172 ± 0.012	0.028 ± 0.020	0.032 ± 0.012	0.015 ± 0.021
J0710	0.108 ± 0.017	0.015 ± 0.019	0.093 ± 0.012	0.018 ± 0.027
J0720	0.232 ± 0.022	0.103 ± 0.020	0.033 ± 0.008	0.052 ± 0.019
J0730	0.159 ± 0.019	-0.076 ± 0.023	0.024 ± 0.015	-0.034 ± 0.022
J0740	0.309 ± 0.017	0.022 ± 0.019	0.086 ± 0.013	0.057 ± 0.036
J0750	0.100 ± 0.016	0.062 ± 0.020	0.083 ± 0.011	0.143 ± 0.012
J0760	0.143 ± 0.018	0.125 ± 0.024	0.086 ± 0.019	0.045 ± 0.038
J0770	0.190 ± 0.019	0.045 ± 0.021	0.054 ± 0.016	0.065 ± 0.026
J0780	0.164 ± 0.017	0.056 ± 0.024	0.099 ± 0.018	0.055 ± 0.034
J0790	0.170 ± 0.014	0.102 ± 0.022	-0.006 ± 0.012	0.053 ± 0.021
J0800	0.044 ± 0.016	0.039 ± 0.023	0.029 ± 0.026	0.014 ± 0.013
J0810	0.047 ± 0.015	0.027 ± 0.025	0.023 ± 0.025	0.001 ± 0.012
J0820	0.049 ± 0.021	0.007 ± 0.022	0.062 ± 0.026	0.031 ± 0.019
J0830	0.095 ± 0.018	0.068 ± 0.023	0.052 ± 0.018	0.058 ± 0.023
J0840	0.126 ± 0.022	0.098 ± 0.023	0.036 ± 0.023	0.061 ± 0.020
J0850	0.103 ± 0.023	0.057 ± 0.024	0.014 ± 0.025	0.008 ± 0.020
J0860	0.117 ± 0.017	0.050 ± 0.006	0.078 ± 0.015	0.036 ± 0.035
J0870	0.300 ± 0.022	0.067 ± 0.023	0.241 ± 0.017	0.036 ± 0.037
J0880	0.293 ± 0.022	0.177 ± 0.024	0.240 ± 0.029	0.031 ± 0.047
J0890	0.247 ± 0.021	0.182 ± 0.032	0.213 ± 0.021	0.178 ± 0.041
J0900	0.173 ± 0.018	0.221 ± 0.030	0.183 ± 0.019	0.240 ± 0.040
J0910	0.128 ± 0.020	0.297 ± 0.027	0.203 ± 0.026	0.143 ± 0.038
J1007	0.179 ± 0.018	0.182 ± 0.024	0.274 ± 0.045	0.074 ± 0.037
uJPAS	0.111 ± 0.036	0.162 ± 0.036	0.156 ± 0.058	0.002 ± 0.048
gSDSS	0.092 ± 0.011	0.060 ± 0.016	0.154 ± 0.013	0.095 ± 0.019
rSDSS	0.000 ± 0.000	0.000 ± 0.000	0.000 ± 0.000	0.000 ± 0.000
iSDSS	0.007 ± 0.010	0.015 ± 0.022	0.093 ± 0.021	0.014 ± 0.031

Table 4. Stellar population properties of model templates

#	f_{dust}	$E(B-V)$ [mag]	$\log U$	t_{burst} [Myr]	t_{main} [Myr]	f_{burst}	τ_{burst} [Myr]	τ_{main} [Myr]	t_{mass} [Myr]	Z	SFR [M$_\odot$ yr^{-1}]	M_* [10^9 M$_\odot$]
01	0.00	0.2	-3.0	100	2000	0.020	50	2000	729	0.008	2.67	2.28
02	0.50	0.5	-3.0	200	5000	0.050	50	2000	2224	0.020	2.15	8.05
03	0.00	0.2	-3.0	500	8000	0.050	200	500	6576	0.020	0.57	13.42
04	0.10	0.0	-3.0	200	5000	0.020	100	2000	2297	0.008	0.72	2.38
05	0.20	0.5	-3.0	100	8000	0.050	50	2000	4238	0.008	1.16	3.24
06	0.00	0.3	-1.0	500	8000	0.020	50	500	6833	0.020	0.01	251.58
07	0.20	0.2	-3.0	1000	8000	0.100	200	2000	4130	0.020	3.44	47.90
08	0.00	0.2	-3.0	500	5000	0.050	200	1000	2961	0.020	0.92	9.33
09	0.20	0.5	-3.0	100	5000	0.020	50	2000	2298	0.020	12.44	35.32
10	0.10	0.4	-3.0	500	8000	0.010	200	500	6909	0.008	0.65	75.24
11	0.95	0.3	-3.0	1000	8000	0.100	50	500	6300	0.020	0.00	18.86
12	0.00	0.0	-3.0	1000	10000	0.020	100	1000	7818	0.020	0.02	18.46
13	0.95	0.0	-3.0	100	8000	0.000	50	500	6995	0.008	0.00	32.42
14	0.00	0.3	-3.0	200	8000	0.100	100	2000	3977	0.008	7.46	21.40
15	0.10	0.4	-3.0	100	2000	0.050	50	1000	828	0.020	2.30	2.46
16	0.20	0.2	-1.0	500	8000	0.010	50	500	6913	0.008	0.00	49.76
17	0.80	0.3	-3.0	500	8000	0.005	100	1000	5958	0.020	1.19	208.87
18	0.10	0.0	-3.0	500	10000	0.010	100	2000	6192	0.020	0.22	6.49
19	0.10	0.5	-3.0	500	5000	0.050	50	2000	2251	0.020	3.28	13.89
20	0.10	0.5	-3.0	200	8000	0.050	50	2000	4272	0.020	8.52	82.49
21	0.10	0.5	-3.0	200	5000	0.050	50	1000	2941	0.020	4.39	47.56
22	0.50	0.3	-3.0	100	10000	0.100	200	1000	6827	0.004	0.02	0.01
23	0.20	0.2	-3.0	100	2000	0.020	50	500	1108	0.020	3.53	9.74
24	0.50	0.3	-3.0	200	8000	0.005	200	500	6947	0.020	0.59	103.01
25	0.20	0.2	-3.0	200	2000	0.100	50	1000	796	0.020	2.40	3.39
26	0.20	0.4	-3.0	200	2000	0.050	200	500	1074	0.020	3.99	8.17
27	0.20	0.4	-3.0	200	5000	0.050	100	2000	2220	0.020	7.19	19.49
28	0.20	0.0	-3.0	200	5000	0.020	50	500	3892	0.020	0.01	0.65
29	0.00	0.4	-1.0	1000	5000	0.100	100	500	3644	0.004	0.07	46.41
30	0.00	0.1	-3.0	200	5000	0.020	50	1000	3052	0.020	0.90	12.07
31	0.00	0.3	-3.0	500	5000	0.050	100	1000	2968	0.020	0.76	11.62
32	0.95	0.2	-3.0	500	8000	0.005	200	1000	5957	0.020	0.57	61.60
33	0.10	0.5	-3.0	200	2000	0.100	100	2000	677	0.008	2.16	1.77
34	0.50	0.5	-3.0	200	2000	0.100	100	500	1018	0.020	7.77	15.89
35	0.00	0.1	-2.5	500	8000	0.010	100	1000	5924	0.020	0.37	59.19
36	0.00	0.2	-2.5	1000	8000	0.005	200	500	6958	0.008	0.05	147.79
37	0.20	0.0	-3.0	500	5000	0.100	200	1000	2794	0.008	0.22	1.65
38	0.00	0.3	-3.0	500	8000	0.005	100	1000	5958	0.020	1.11	194.79
39	0.20	0.3	-3.0	200	10000	0.005	50	2000	6224	0.004	1.44	38.80
40	0.00	0.3	-3.0	1000	8000	0.100	200	2000	4130	0.020	0.66	9.15
41	0.10	0.5	-3.0	500	5000	0.020	200	500	3901	0.020	2.02	111.96
42	0.00	0.3	-1.0	1000	5000	0.050	50	500	3820	0.004	0.01	3.65
43	0.95	0.0	-3.0	100	10000	0.000	50	500	8996	0.008	0.00	22.92
44	0.00	0.2	-2.5	1000	8000	0.050	50	1000	5704	0.004	0.04	8.11
45	0.00	0.3	-3.0	1000	8000	0.100	100	500	6291	0.020	0.00	33.77
46	0.00	0.0	-3.0	1000	10000	0.020	50	1000	7819	0.008	0.00	2.76
47	0.00	0.3	-3.0	200	8000	0.005	50	1000	5953	0.008	0.07	7.95
48	0.00	0.5	-3.0	200	5000	0.100	200	2000	2081	0.020	14.56	20.45
49	0.00	0.2	-3.0	1000	8000	0.050	200	1000	5691	0.020	0.13	15.82
50	0.00	0.3	-3.0	200	10000	0.020	50	1000	7771	0.008	1.06	68.77

Table 5. Observables measured on model templates

#	log $L_\nu(g)$ [W m^{-2}]	u-r [AB mag]	g-i [AB mag]	β	$D_n(4000)$	EW([O II]) [nm]	EW([O III]) [nm]	EW(Hα) [nm]
01	21.69	0.82	0.23	-2.04	1.12	6.915	2.788	11.634
02	21.51	1.59	0.83	-1.44	1.25	0.775	0.208	1.488
03	21.46	1.67	0.83	-1.73	1.32	2.511	0.439	2.262
04	21.46	0.90	0.32	-2.24	1.17	6.636	2.024	6.495
05	21.14	1.30	0.68	-1.66	1.18	2.363	1.118	4.762
06	22.41	2.59	1.24	0.85	1.70	0.008	0.052	0.072
07	22.19	1.70	0.83	-1.80	1.36	1.968	0.346	1.790
08	21.58	1.56	0.77	-1.80	1.30	2.899	0.545	2.924
09	22.15	1.49	0.84	-1.53	1.23	1.780	0.520	3.638
10	21.90	2.39	1.26	-1.33	1.59	0.861	0.188	0.496
11	21.38	2.53	1.19	3.50	1.72	0.004	0.000	0.002
12	21.44	2.35	1.09	-0.85	1.82	0.618	0.057	0.199
13	21.77	2.22	1.06	0.84	1.78	0.015	0.002	0.005
14	22.19	1.08	0.46	-1.86	1.16	4.293	1.739	6.975
15	21.43	1.15	0.55	-1.67	1.17	2.766	0.858	6.533
16	21.85	2.35	1.15	0.07	1.68	0.007	0.092	0.080
17	22.35	2.53	1.28	-1.37	1.72	0.105	0.013	0.053
18	21.24	1.63	0.81	-2.09	1.39	3.220	0.458	1.918
19	21.69	1.71	0.89	-1.47	1.28	1.868	0.467	3.175
20	22.30	1.73	0.91	-1.34	1.26	1.208	0.299	2.015
21	22.09	1.82	0.96	-1.31	1.29	1.060	0.248	1.618
22	19.11	0.69	0.26	-2.16	1.08	2.322	1.896	8.827
23	21.97	1.22	0.55	-1.89	1.22	2.628	0.609	3.789
24	22.05	2.43	1.24	-1.35	1.70	0.115	0.012	0.055
25	21.71	1.00	0.38	-1.89	1.17	2.919	0.758	5.317
26	21.77	1.38	0.69	-1.64	1.22	2.058	0.555	3.899
27	22.02	1.35	0.70	-1.65	1.21	2.070	0.573	3.957
28	20.34	1.69	0.80	-1.86	1.39	1.063	0.150	0.638
29	22.02	2.26	1.08	1.14	1.50	0.003	0.080	0.095
30	21.73	1.47	0.72	-1.91	1.30	2.945	0.522	2.596
31	21.55	1.84	0.91	-1.56	1.36	1.889	0.338	1.850
32	21.91	2.34	1.18	-1.70	1.66	0.042	0.005	0.021
33	21.35	1.22	0.50	-1.63	1.17	3.207	1.501	7.322
34	22.02	1.47	0.74	-1.46	1.23	0.822	0.236	1.794
35	22.00	2.22	1.06	-1.57	1.62	0.610	0.227	0.500
36	22.29	2.41	1.20	0.25	1.77	0.177	0.111	0.138
37	21.17	1.15	0.42	-2.11	1.24	3.824	1.015	3.133
38	22.32	2.51	1.27	-1.35	1.71	0.773	0.094	0.391
39	21.95	1.89	0.95	-1.67	1.39	1.052	0.407	1.279
40	21.39	1.81	0.91	-1.66	1.37	2.274	0.419	2.271
41	22.11	2.47	1.32	-1.21	1.55	0.698	0.111	0.560
42	20.94	2.20	1.05	1.14	1.54	0.005	0.105	0.113
43	21.53	2.29	1.10	0.39	1.84	0.017	0.002	0.005
44	21.28	2.07	0.98	-0.45	1.51	0.185	0.221	0.346
45	21.65	2.50	1.17	2.67	1.69	0.113	0.014	0.063
46	20.73	2.13	1.00	-0.25	1.70	0.627	0.098	0.207
47	21.08	2.20	1.14	-1.43	1.54	0.998	0.217	0.561
48	22.10	1.25	0.68	-1.56	1.16	2.919	0.983	7.567
49	21.41	2.26	1.09	-1.34	1.61	0.931	0.117	0.503
50	22.07	1.84	0.95	-1.56	1.35	1.223	0.330	0.974